Electronic Supplementary Material (ESI) for ChemComm.
This journal is © The Royal Society of Chemistry 2021

**Supporting Information for**

# Conductive Interface Promoted Bifunctional Oxygen Reduction/Evolution Activity in Ultra-low Precious Metal based Hybrid Catalyst

Shreya Sarkar,[1,2] Merin Varghese,[1,2] C. P. Vinod[3] and Sebastian C. Peter[1,2]

[1]*New Chemistry Unit, Jawaharlal Nehru Centre for Advanced Scientific Research, Bangalore, India*

[2]*School of Advanced Materials, Jawaharlal Nehru Centre for Advanced Scientific Research, Bangalore 560 064, India*

[3]*Catalysis and Inorganic Chemistry Division, CSIR-National Chemical Laboratory, Dr. Homi Bhabha Road, Pune, 411008*

## Experimental Section

### 1. Synthesis

**1.1.** *Chemicals*: Nickel chloride hexahydrate ($NiCl_2.6H_2O$), red phosphorus (P30), urea and polyvinyl-2-pyrrolidone (PVP) were purchased from SDFCL. Potassium chloroplatinate ($K_2PtCl_4$) and palladium acetyl acetonate ($Pd(acac)_2$) ($Pd(C_6H_{14}O_4)$ were purchased from Alfa Aesar. All the reagents were used without further purification. Distilled water (DI, 18.2 mΩ·cm) was used throughout the syntheses and measurements.

**1.2.** *Synthesis of $Ni_{12}P_5$*: A quantity of 1.425 g of $NiCl_2.6H_2O$ was dissolved in 33 ml of DI water by stirring. Urea (0.84 g) and PVP (0.3 g) were added during stirring. To this mixture, 1.5 g of red phosphorous was added and continued stirring for 20 min. The solution was transferred to a 50 ml autoclave, and reaction was kept at 180 ºC for 24 hrs. After cooling, the obtained precipitate was washed using ethanol and dried at 70 ºC under vacuum.

**1.3.** *Reduction of $K_2PtCl_4$ and $Pd(acac)_2$ on $Ni_{12}P_5$ surface*: The reduction of $K_2PtCl_4$ was performed in-situ by using triethylene glycol as the solvent which is a mild reducing agent. An amount of 150 mg of previously synthesized $Ni_{12}P_5$ was dispersed in 100 ml of triethyleneglycol by sonication for 10 min. To the above solution, stoichiometric amounts of $K_2PtCl_4$ and $Pd(acac)_2$ were added and stirred for 6 hours at 80 ºC under atmospheric conditions. After cooling, the precipitate was washed with ethanol and dried under vacuum at 70 ºC. This procedure was repeated by increasing the total metal wt % loading from 5 to 7.5 and 10 with composition ratio between Pt:Pd as 1:1 wherein the catalysts are designated as $Pt_1Pd_1(5)/Ni_{12}P_5$, $Pt_1Pd_1(7.5)/Ni_{12}P_5$ and $Pt_1Pd_1(10)/Ni_{12}P_5$. The best active

catalyst was the one with 7.5 % metal loading. For the $Pt_1Pd_1(7.5)/Ni_{12}P_5$ catalyst we varied the ratio of Pt:Pd as 1:2 ($Pt_1Pd_2(7.5)/Ni_{12}P_5$) and 2:1 ($Pt_2Pd_1(7.5)/Ni_{12}P_5$).

Mechanism: Using a mild hydrothermal route of synthesis we achieved the formation of agglomerated $Ni_{12}P_5$ nanostructures. In our experiment $NiCl_2.6H_2O$ was directly phosphorized at 180 ºC in the presence of red P in a PTFE lined autoclave containing water as the solvent. $Ni_{12}P_5$ forms through a direct redox reaction between Ni and dissolved P species: $Ni^0 + P^0 \rightarrow (Ni^{1.25+})_{2.4}P^{3-}$, where Ni has a formal charge of $1.25^+$, while the charge of P is $3^-$. The driving force of the reaction is the transfer of electrons from the electropositive Ni metal to the electronegative P. With the reaction processing, urea decomposed gradually and the reaction solution became alkaline. In this basic system with suitable temperature, as a relatively active reducing agent, red P could easily react with OH to produce active electrons, which would reduce TM ions to the atoms. These newborn metal atoms were pretty active, immediately they could directly react with red P to form $Ni_{12}P_5$.

## 2. Characterization

### 2.1. PXRD measurements

The PXRD measurements at room temperature were carried out on a Rigaku miniflex X-ray diffractometer using Cu-*Kα* as the X-ray source (λ = 1.5406 Å). The instrument is equipped with a position sensitive detector in the angular range $20^o \leq 2\theta \leq 90^o$ with the step size $0.02^o$ and scan rate of 1 sec/step calibrated against corundum standard. The experimental patterns were compared to the pattern simulated from Pearson's Crystal database.

Experimental powder XRD patterns of the samples prepared by solvothermal and subsequent aqueous-phase reactions were compared with the simulated patterns as shown in **Figure S1**. A set of prominent diffraction peaks at 2θ = 32.86º, 35.87º, 37.9º, 40.8º, 41.64º, 41.92º, 44.6º, 47.16º, 48.62º, 54.62º, 56.28º were consistent with (310), (301), (112), (202), (400), (330), (240), (312), (510), (431) and (242) crystal planes of tetragonal $Ni_{12}P_5$ nanocrystals. For the $Pt/Ni_{12}P_5$ and $PtPd/Ni_{12}P_5$ samples, the $Ni_{12}P_5$ structure retained with a shift towards higher 2θ indicating the successful introduction of noble metals in the $Ni_{12}P_5$ crystal lattice (**Figure S2**). XRD peaks at 39.8, 46.2, and 67.2° are assigned to the (111), (200), and (220) diffraction peaks for face-centered cubic (fcc) Pt, respectively whereas those at 40.12, 46.6 and 68.1 are assigned to face-centered cubic (fcc) Pd. However, for $Pt/Ni_{12}P_5$, $Pt_1Pd_1(5)/Ni_{12}P_5$ and $Pt_1Pd_1(7.5)/Ni_{12}P_5$ no distinct property of the fcc Pt and Pd

can be identified but at around 2θ = 40° broadening of the peaks maybe due to the presence of both phases or indicating the formation of metal alloy nanoparticles. The strong peaks of $Ni_{12}P_5$ (202) and $Ni_{12}P_5$ (400) may cover or integrate the peaks of Pt and Pd, forming the broadened peaks at approximately 40 and 46°. This result may be ascribed to the low amount of Pt and Pd loading and small size as well as the much stronger diffraction peak for $Ni_{12}P_5$. On the contrary, when total metal loading was increased to 10 wt.%, $Ni_{12}P_5$ completely disrupted with majorly PtPd alloy formation.

### 2.2. Transmission electron microscopic imaging

TEM images and selected area electron diffraction patterns were collected using a JEOL JEM-2010 TEM instrument and color mapping was done in TECHNAI. The samples for these measurements were prepared by sonicating the nanocrystalline powders in ethanol and drop-casting a small volume onto a carbon-coated copper grid.

TEM image shows that $Ni_{12}P_5$ have agglomerated structures with average size between 80-100 nm whereas the as deposited PtPd in $Ni_{12}P_5$ form nanoclusters of particle size less than 5 nm (**Figsures S3a** and **S3c**). **Figure S3b** shows the SAED pattern corresponding to (112), (330) and (420) crystallographic planes of $Ni_{12}P_5$. In **Figure S3d** the SAED pattern for $Pt_1Pd_1(7.5)/Ni_{12}P_5$ however was indexed to (111), (200) and (220) planes of PtPd alloy with the last ring corresponding to $Ni_{12}P_5$. This gives a hint to the probable interaction between the PtPd metal deposited on $Ni_{12}P_5$ nanoparticles.

### 2.3. Scanning electron microscopy and EDAX/Elemental analysis

The FESEM images shows that pristine $Ni_{12}P_5$ have agglomerated morphology (**Figure S4**) whereas that for $Pt_1Pd_1(7.5)/Ni_{12}P_5$ small nanoparticles cluster was observed on these agglomerated sheets (**Figure S5**). The EDX measurement was performed using FEI NOVA NANOSEM 600 scanning electron microscope equipped with an energy-dispersive X-ray spectroscopy (EDAX) instrument (Bruker 129 eV EDAX instrument). Data was acquired by using an accelerating voltage of 20 kV and typical time taken for data accumulation is 100 s. The elemental analyses were performed using the P/B-ZAF standardless method (where, P/B = peak to background model, Z = atomic no. correction factor, A = absorption correction factor and F = fluorescence factor) for C, N, O, Co at multiple areas on the sample coated Si wafer. EDAX elemental analysis showed 68.4 atomic wt.% of Ni and 31.6 atomic wt.% of P in $Ni_{12}P_5$ is in good agreement with the expected stoichiometry of 12:5 (**Figure S4**). $Pt_1Pd_1(7.5)/Ni_{12}P_5$ the atomic wt.% of Pd and Pt was found to be 17.95 and 11.07

respectively with 37.46 and 23.74 atomic wt. % of Ni and P respectively (**Figure S5**). This gives an indication the PtPd has a close stoichiometry to that of $Pd_{0.5}Pt_{0.5}$ fcc alloy.

### 2.4. X-ray photoelectron spectroscopy

XPS measurements were carried out using Thermo K-alpha+ spectrometer using micro focused and monochromated Al Kα radiation with energy 1486.6 eV. The pass energy for spectral acquisition was kept at 50 eV for individual core-levels. The electron flood gun was utilized for providing charge compensation during data acquisition. Further, the individual core-level spectra were checked for charging using C1s at 284.6 eV as standard and corrected if needed. The peak fitting of the individual core-levels were done using XPSpeak 41 software with a Shirley type background. XPS spectra were measured to study the valence state, chemical composition and electronic interactions between the deposited metal nanoparticles and $Ni_{12}P_5$ (**Figures S6-S10**). **Figure S6a** shows the Ni 2p spectra for $Ni_{12}P_5$ where the two peaks at 853.6 eV and 873 eV were observed corresponding to the $2p_{3/2}$ and $2p_{1/2}$ spin-orbit couplings for $Ni^{\delta+}$ in $Ni_{12}P_5$. The satellite peaks of Ni at 861.1 and 879.6 eV are also detected. The peaks at 133 eV and 134 eV corroborates with the $P^{\delta-}$ peak in $Ni_{12}P_5$ (**Figure S6b**). **Figures S6-S10** shows the XPS spectra of Ni 2p, P 2p, Pd 3d and Pt 4f for $Pt/Ni_{12}P_5$, $Pt_1Pd_1(5)/Ni_{12}P_5$, $Pt_1Pd_1(7.5)/Ni_{12}P_5$ and $Pt_1Pd_1(10)/Ni_{12}P_5$. Ni binding energy in these XPS spectra is shifted to higher energy with respect to that of bare $Ni_{12}P_5$ with concomitant shift to lower energy for P. The spin-orbit coupling due to Pt 4f and Pd 3d in PtPd alloy is also shown in each figure. For example, in the case of $Pt_1Pd_1(7.5)/Ni_{12}P_5$, two peaks at 71.2 eV and 74.5 eV can be assigned to the corresponding to Pt $4f_{7/2}$ and $4f_{5/2}$ states whereas that at 335.8 eV and 341eV is assigned to Pd $3d_{5/2}$ and $3d_{3/2}$ states.

### 2.5. X-ray Absorption Spectroscopy

X-ray absorption near edge spectroscopy (XANES) and quick-Extended X-ray Absorption Fine Structure (quick-EXAFS) experiments at 300 K were performed at PETRA III, beamline P64, of DESY, Germany. Measurements of Pd-K, and Bi-$L_{III}$ edges at ambient pressure were performed in fluorescence as well as transmission mode using gas ionization chambers to monitor the incident and transmitted X-ray intensities. Monochromatic X-rays were obtained using a Si (111) double crystal monochromator which was calibrated by defining the inflection point (first derivative maxima) of Cu foil as 8980.5 eV. The beam was focused by employing a Kirkpatrick-Baez (K-B) mirror optic. A rhodium- coated X-ray mirror was used to suppress higher order harmonics. A CCD detector was used to record the

transmitted signals. Pellets for the ex-situ measurements were made by homogeneously mixing the sample with an inert cellulose matrix to obtain an X-ray absorption edge jump close to one.

The EXAFS fitting of $Ni_{12}P_5$ and PtPd/$Ni_{12}P_5$ compounds was performed by considering appropriate theoretical models of $Ni_{12}P_5$ constructed by using FEFF 6code. EXAFS data of the catalyst materials were fitted simultaneously with k-weights of 1, 2, and 3. The $S_o^2$ value was fixed to 1 prior to the fitting procedure. The EXAFS data were Fourier transformed in the range of 4−13.8 $Å^{-1}$. Data were fitted in R-space between 1 and 3 Å for all the samples. The fitting parameters consist of bond length change between atoms (ΔR), change in energy scale between data and theory ($\Delta E_0$), and mean-square displacement of the bond length ($\sigma^2$).

**3. Electrochemical measurements**

All the electrochemical measurements were performed by using CHI 760E electrochemical workstation in three electrode configurations. Hg/HgO was used as reference electrode for alkaline media and saturated calomel electrode for acidic media and graphite rod as counter electrode. All the potentials reported here were corrected to reversible hydrogen electrode (RHE). Electrocatalytic activity was studied in $O_2$ saturated 0.1M KOH and 0.1M $HClO_4$ using rotating disk electrode (RDE) and rotating ring disk electrode (RRDE) for ORR. The Pt ring electrode was operated at a constant potential of 0.5V.

Catalyst slurry was prepared by dispersing 2.4 mg of the catalysts and 0.6 mg vulcan in 200ul of 1:3 IPA and $H_2O$ mixture. This dispersion was sonicated well to obtain homogenous catalyst slurry. ORR studies were performed on rotating disk electrode (RDE), fitted with glassy carbon of area 0.0706 $cm^2$. Working electrodes were prepared by drop casting 10 µl of catalyst slurry on RDE and dried under infrared lamp to obtain uniform coating. Fiveµl of nafion (1wt%) was casted on it just before drying. Ten µl of this slurry was coated on RDE and 20 µl on RRDE to obtain ~ 0.15mg/$cm^2$.

Koutecky-Levich (K-L) plots were obtained from the K-L equation[4]

$$\frac{1}{j} = \frac{1}{j_d} + \frac{1}{j_k} + \frac{1}{j_f} \quad (Eqn.\ S1)$$

where $j$ is the measured current density, $j_k$ is the kinetic current density, $j_d$ is the diffusion (mass-transfer) limited current density and $j_f$ is the film diffusion current. Here, $j_f$can be

neglected as the amount of Nafion is significantly low and hence will not affect the limiting current density. In the laminar flow region, the diffusion current density is a function of the rotational velocity and hence the above equation may be approximated as follows:

$$\frac{1}{j} = \frac{1}{j_d} + \frac{1}{j_k} = -\frac{1}{nFkC^b} - \frac{1}{0.62nAFD^{\frac{3}{2}}\nu^{-\frac{1}{6}}C^b\omega^{\frac{1}{2}}} \quad (Eqn.\ S2a)$$

$$j_d = 0.62nFAC^0 D_{O_2}^{2/3}\nu^{-1/6}\omega^{1/2} \quad (Eqn.\ S2b)$$

where F is the Faraday constant (96485 C $mol^{-1}$), k is the rate constant for $O_2$ reduction, *n* is the number of electrons, *A* is the area of the electrode, $C^0$ is the concentration of $O_2$ in the bulk ($1.22 \times 10^{-6}$ mol $mL^{-1}$), D is the diffusion coefficient of $O_2$ ($1.93 \times 10^{-5}$ $cm^2s^{-1}$), v is the kinematic viscosity of solution (0.01 $cm^2s^{-1}$), and ω is the rotating speed (rad $s^{-1}$). From the K–L equation, the reciprocal of square root of rotating speed ($\omega^{-1/2}$) and the reciprocal of measured current density ($j^{-1}$) should exhibit a linear relationship.[5] The value obtained for the kinetic current was independent of diffusion and could be used to evaluate the intrinsic activity of the catalysts. The plot of the inverse of current density (1/*j*) as a function of the inverse of the square root of the rate ($\omega^{-1/2}$), at a particular potential obtained from the hydrodynamic voltammogram, assists in the evaluation of the useful kinetic parameters such as kinetic current density ($j_k$), number of electron transfer (*n*) and rate constant for ORR (*k*).

Number of electron transfer and $H_2O_2$ yield were measured using rotating ring disk electrode (RRDE) with ring as platinum and disk as glassy carbon (0.12 $cm^2$), (CF: 0.41). Twentyμl of sample was drop casted on disk region and nafion was added just before drying. The fraction of current due to $HO^{2-}$ that is recorded by the ring electrode ($X_{HO2-}$) and the

corresponding electron transfer numbers during ORR ($ne^-$) can be determined from the following equation.[6]

$$X_{HO_2^-} = \frac{2I_R/N}{I_D + I_R/N} \quad (Eqn.\ S3)$$

$$n_{e^-} = \frac{4I_D}{I_D + I_R/N} \quad (Eqn.\ S4)$$

where $I_R$ is the ring current, $I_D$ is the disk current, and N is the collection efficiency.

The ORR equations and equilibrium potentials (vs. SHE) in acidic and alkaline media are shown in EqnS5-S10.

**A. Alkaline media**

$O_2 + 2H_2O + 4e^- \leftrightarrow 4OH^-$; $E^0 = 0.401$ V vs SHE (Eqn. S5)

or,

(a) $O_2 + H_2O + 2e^- \leftrightarrow HO_2^- + OH^-$; $E^0 = -0.076$ V vs SHE (Eqn. S6)

followed by either further reduction through,

(b1) $HO_2^- + H_2O + 2e^- \leftrightarrow 3OH^-$; $E^0 = 0.878$ V vs SHE (Eqn. S7a)

Or disproportionation by

(b2) $2HO_2^- \leftrightarrow 2OH^- + O_2$ (Eqn. S7b)

**B. Acidic media**

$O_2 + 4H^+ + 4e^- \leftrightarrow 2H_2O$; $E^0 = 1.229$ V vs SHE (Eqn. S8)

or,

(a) $O_2 + 2H^+ + 2e^- \leftrightarrow H_2O_2$; $E^0 = 0.695$ V vs SHE (Eqn. S9)

Followed by either,

(b1) $H_2O_2 + 2H^+ + 2e^- \leftrightarrow 2H_2O$; $E^0 = 1.776$ V vs SHE (Eqn. S10a)

or,

(b2) $2H_2O_2 \leftrightarrow 2H_2O + O_2$ (Eqn. S10b)

All the electrochemical OER measurements were done in a 3-electrode set-up comprising of a glassy carbon as the working electrode (GCE), graphite rod counter electrode and mercury/mercuric oxide electrode (MMO) reference electrode for alkaline media. The catalyst ink was prepared using 2.4 mg of the catalysts and 0.6 mg vulcan in 200ul of 1:3 IPA and $H_2O$ mixture. Ten µL of the catalyst ink was drop casted on the commercial 3 mm glassy carbon electrode. Commercial $IrO_2$ (Sigma Aldrich) were used for comparison of activity with the reported electrocatalysts. Linear sweep voltammetry (LSV) was recorded for OER at a scan rate of 5 mV $s^{-1}$ at 25 °C. Electrochemical impedance studies were performed in the frequency range from 10 mHz to 100 kHz at different applied DC potentials for different reactions depending on their onset potential values. The electrolyte solution was deaerated by purging nitrogen gas into the solution at least for 30 min before each experiment.

**4. Fabrication of MEA for single cell analysis**

For fabricating the membrane electrode assembly (MEA), the proton conducting membrane was fabricated by using Nafion 212 membrane. The pre-treatment of the membrane was performed in 5% $H_2O_2$ solution at 80 °C for 45 minutes followed by 1M $H_2SO_4$ and distilled (DI) water and at 80 °C. The pre-treated membrane was stored in DI water for further use while assembling the MEA. The electrode was prepared by brush coating of catalyst slurry on the top surface of a carbon gas diffusion layer (GDL) (carbon

cloth). For the cathode, the catalyst ink was made by mixing $Pt_1Pd_2(7.5)/Ni_{12}P_5$ and 5 wt.% Nafion dispersion in IPA. A Nafion to catalyst ratio of 0.5 was kept in the catalyst ink. The ink was applied onto the GDL. For the anode, Pt/C (40 wt.%) was used as the catalyst. The loadings of the catalyst for both the anode and cathode were measured to be 0.50 and 3.0 mg $cm^{-2}$, respectively. The MEA was prepared by using the pre-treated Nafion membrane between the anode and cathode electrodes by maintaining an active area of 5 $cm^2$. The assembly was hot pressed with a pressure of 1000 psi for 3 min at temperature of 140 °C. The single cell performance of the prepared MEA was assessed by using a 5 $cm^2$ test fixture procured from Fuel Cell Technologies, Inc, USA, by connecting to a fuel cell test station. 100 sccm of hydrogen and 200sccm of oxygen were supplied to the anode and cathode, respectively, without applying any back pressure. The complete measurement has been done under 100 % relative humidity condition by operating at a cell temperature of 60 °C.

**Tables**

**Table S1.** Summary of the various synthesized electrocatalysts with their respective onset potential, $E_{1/2}$ and electron transfer number.

| Catalyst | Onset (V vs. RHE) | $E_{1/2}$ (V vs. RHE) | Number of electrons |
|---|---|---|---|
| $Ni_{12}P_5$ | 0.83 | 0.67 | 3.1 |
| $Pt/Ni_{12}P_5$ | 0.9 | 0.72 | 3.7 |
| $Pt_1Pd_1(5)/ Ni_{12}P_5$ | 0.95 | 0.83 | 3.6 |
| $Pt_1Pd_1(7.5)/ Ni_{12}P_5$ | 0.98 | 0.9 | 3.9 |
| $Pt_1Pd_1(10)/ Ni_{12}P_5$ | 0.95 | 0.85 | 3.7 |
| $Pt_1Pd_2(7.5)/ Ni_{12}P_5$ | 1.003 | 0.95 | 3.9 |
| $Pt_2Pd_1(7.5)/ Ni_{12}P_5$ | 0.97 | 0.88 | 3.8 |

**Table S2.** Electrochemical impedance parameters of the catalysts for ORR in 0.1M KOH.

| Catalyst | $R_e$ (Ω) | $R_{CT}$ (Ω) | $Z_w$ | D ($cm^2s^{-1}$) |
|---|---|---|---|---|
| $Ni_{12}P_5$ | 8.86 | 143 | 0.0764 | 1.98E-16 |
| $Pt/Ni_{12}P_5$ | 7.759 | 115 | 0.0483 | 1.85E-16 |
| $Pt_1Pd_1(5)/ Ni_{12}P_5$ | 5.156 | 86.2 | 0.03933 | 1.74E-15 |
| $Pt_1Pd_1(7.5)/ Ni_{12}P_5$ | 4.002 | 59.95 | 0.01318 | 1.43E-15 |
| $Pt_1Pd_1(10)/ Ni_{12}P_5$ | 6.543 | 98.4 | 0.0356 | 1.56E-15 |
| $Pt_1Pd_2(7.5)/ Ni_{12}P_5$ | 2.008 | 49.85 | 0.0124 | 1.24E-15 |
| $Pt_2Pd_1(7.5)/ Ni_{12}P_5$ | 3.132 | 68.83 | 0.0324 | 1.38E-15 |

**Table S3.** EXAFS fitting parameters.

| Catalyst | Shell | N | R (Å) | $\sigma^2$ | $\Delta E_0$ |
|---|---|---|---|---|---|
| $Ni_{12}P_5$ | Ni-P | 3.5 | 2.24 | 0.009 | 0.5 |
| | Ni-Ni | 5.4 | 2.63 | 0.006 | 0.6 |
| $Pt/Ni_{12}P_5$ | Ni-P | 3.4 | 2.24 | 0.007 | 2.3 |
| | Ni-Ni | 3.4 | 2.62 | 0.006 | 3.5 |
| $PtPd/Ni_{12}P_5$ | Ni-P | 3.2 | 2.23 | 0.009 | 2.12 |
| | Ni-Ni | 3.2 | 2.62 | 0.008 | 3.2 |

**Table S4.** BET surface area of all the synthesized catalysts.

| Catalyst | Surface area ($m^2/g$) |
|---|---|
| $Ni_{12}P_5$ | 25 |
| $Pt_1Pd_1(5)/Ni_{12}P_5$ | 32 |
| $Pt_1Pd_1(7.5)/Ni_{12}P_5$ | 45 |
| $Pt_1Pd_1(10)/Ni_{12}P_5$ | 27 |
| $Pt_1Pd_2(7.5)/Ni_{12}P_5$ | 64 |
| $Pt_2Pd_1(7.5)/Ni_{12}P_5$ | 44 |

**Table S5.** Electrochemical impedance parameters of the catalysts for ORR in 0.1M $HClO_4$.

| Catalyst | $R_e$ (Ω) | $R_{CT}$ (Ω) | $Z_w$ | D ($cm^2s^{-1}$) |
|---|---|---|---|---|
| $Ni_{12}P_5$ | 4.73 | 105 | 0.0523 | 1.92E-16 |
| $Pt_1Pd_1(7.5)/Ni_{12}P_5$ | 2.78 | 97 | 0.0285 | 1.68E-15 |
| $Pt_1Pd_2(7.5)/Ni_{12}P_5$ | 1.87 | 64 | 0.0168 | 1.32E-15 |
| $Pt_2Pd_1(7.5)/Ni_{12}P_5$ | 2.54 | 78 | 0.0315 | 1.54E-15 |

**Table S6.** Electrochemical impedance parameters of the catalysts for OER in 0.1M KOH.

| Catalyst | $R_e$ (Ω) | $R_{CT}$ (Ω) | $Z_w$ |
|---|---|---|---|
| $Ni_{12}P_5$ | 3.86 | 287 | 0.0514 |
| $IrO_2$ | 3.24 | 235 | 0.0536 |
| $Pt_1Pd_1(7.5)/Ni_{12}P_5$ | 2.734 | 160 | 0.0275 |
| $Pt_1Pd_2(7.5)/Ni_{12}P_5$ | 1.98 | 135 | 0.0184 |
| $Pt_2Pd_1(7.5)/Ni_{12}P_5$ | 2.563 | 175 | 0.0293 |

**Table S7.** Summary of the various reported noble metal based electrocatalysts with their respective onset potential, $E_{1/2}$ in comparison to our best active electrocatalyst.

| Sl. No. | Catalysts | Onset potential (V vs. RHE) | $E_{1/2}$ (V vs. RHE) | References |
|---|---|---|---|---|
| 1 | PtP | 0.96 | 0.85 | 1 |
| 2 | PtPd nanoalloys | 0.97 | 0.9 | 2 |
| 3 | PtPd nanocubes | 0.96 | 0.89 | 3 |
| 4 | PtPd alloys | 0.9 | 0.85 | 4 |
| 5 | PtPd nanoflowers | 1 | 0.95 | 5 |
| 6 | PtPd nanocrystals | 0.94 | 0.85 | 6 |
| 7 | Au doped PtCo | 0.96 | 0.9 | 7 |
| 8 | Pt doped $Ni(OH)_2$ | 1.023 | 0.9 | 8 |
| 9 | Pt on N,C doped Fe | 0.9 | 0.87 | 9 |
| 10 | Janus Pt-FeNC | 0.94 | 0.9 | 10 |
| 11 | PtNi nanotube | 0.98 | 0.917 | 11 |
| 12 | Ga doped PtNi | 0.98 | 0.95 | 12 |
| 13 | PtCu octahedra | 1.0 | 0.94 | 13 |
| 14 | Mo doped $Pt_3Ni$ | 1.0 | 0.97 | 14 |
| 15 | PtCuCo | - | 0.95 | 15 |
| 16 | Pt-$WO_3$ | 0.95 | 0.87 | 16 |
| 17 | $Fe_xPt$ | 0.98 | 0.95 | 17 |
| 18 | Au@PtPd | 1.01 | 0.92 | 18 |
| 19 | $Pt_2Ni_8$ | 0.92 | 0.9 | 19 |
| 20 | N-doped PtNi | 0.98 | 0.92 | 20 |
| 21 | $Pt_3Ni$ | 0.98 | 0.9 | 21 |
| **22** | **$Pt_1Pd_2/Ni_{12}P_5$** | **1.003** | **0.98** | **This work** |

**Figures**

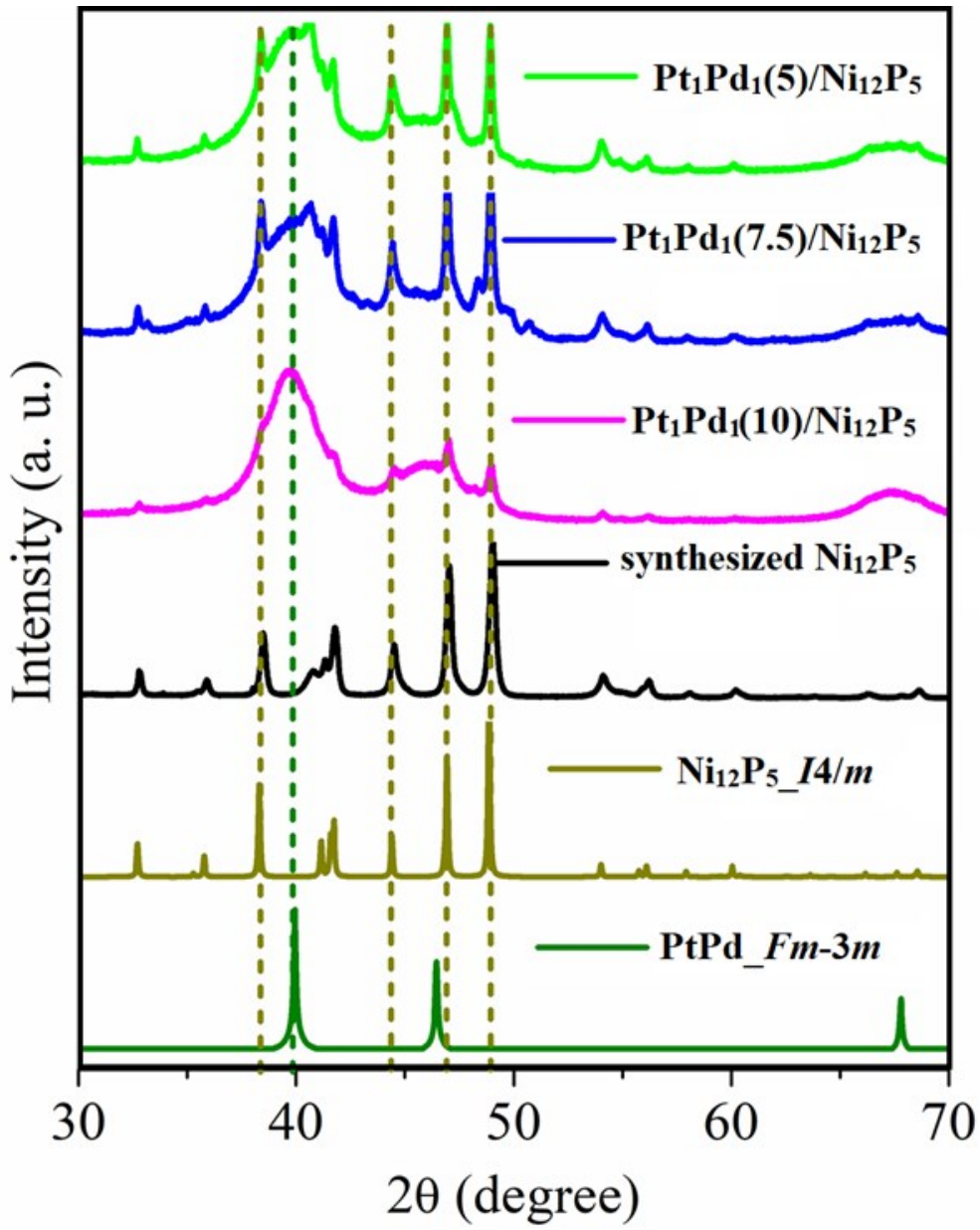


**Figure S1.** Comparison of the PXRD patterns of $Pt_1Pd_1(5)/Ni_{12}P_5$, $Pt_1Pd_1(7.5)/Ni_{12}P_5$, $Pt_1Pd_1(10)/Ni_{12}P_5$, $Pt/Ni_{12}P_5$, and $Ni_{12}P_5$ with simulated patterns of PtPd alloy and tetragonal phase of $Ni_{12}P_5$.

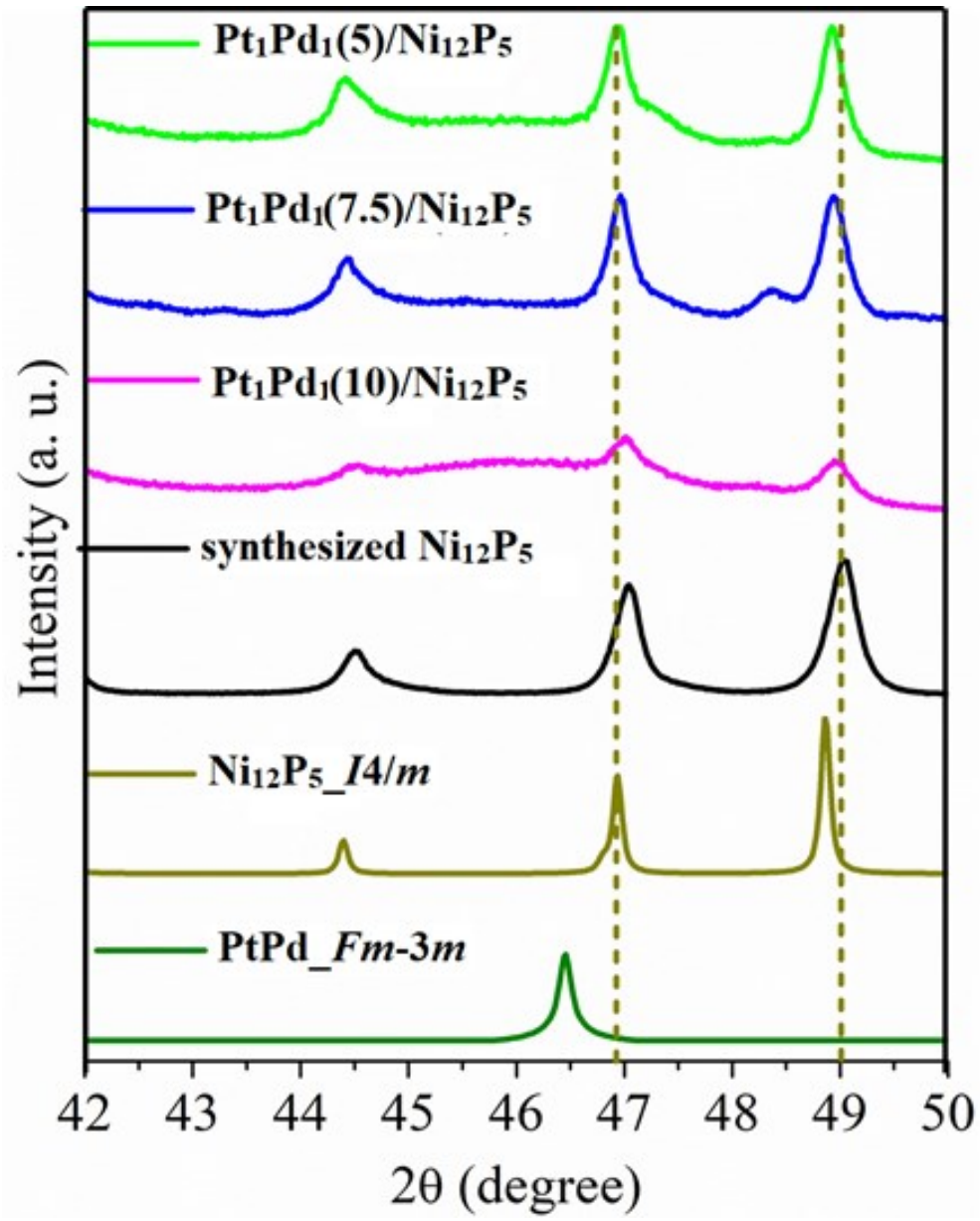


**Figure S2**. Enlarged view of the Comparison of the PXRD patterns of $Pt_1Pd_1(5)/Ni_{12}P_5$, $Pt_1Pd_1(7.5)/Ni_{12}P_5$, $Pt_1Pd_1(10)/Ni_{12}P_5$, $Pt/Ni_{12}P_5$, and $Ni_{12}P_5$ with simulated patterns of PtPd alloy and tetragonal phase of $Ni_{12}P_5$.

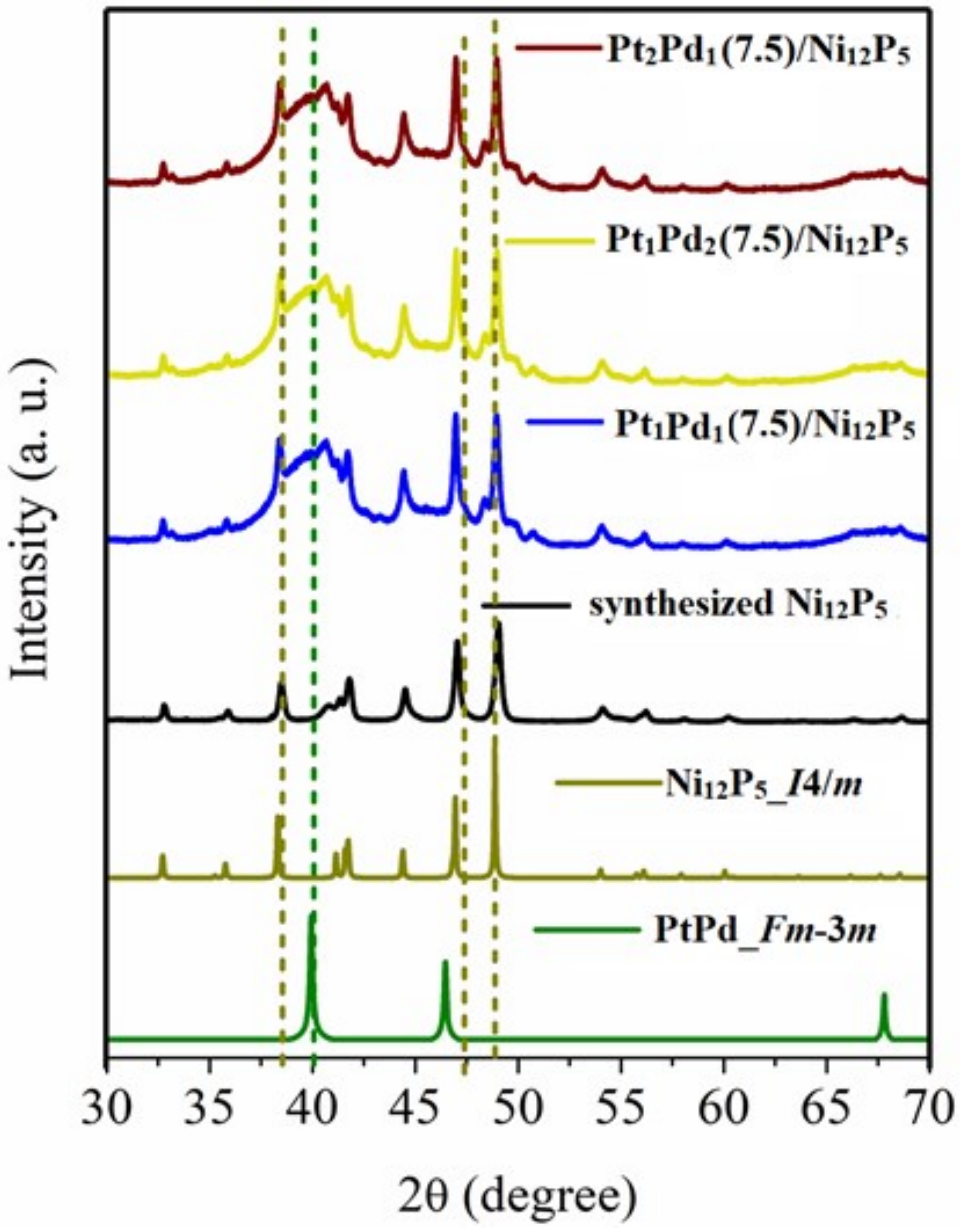


**Figure S3.** Comparison of the PXRD patterns of $Pt_1Pd_1(7.5)/Ni_{12}P_5$, $Pt_1Pd_2(7.5)/Ni_{12}P_5$ and $Pt_2Pd_1(7.5)/Ni_{12}P_5$ with simulated patterns of PtPd alloy and tetragonal phase of $Ni_{12}P_5$.

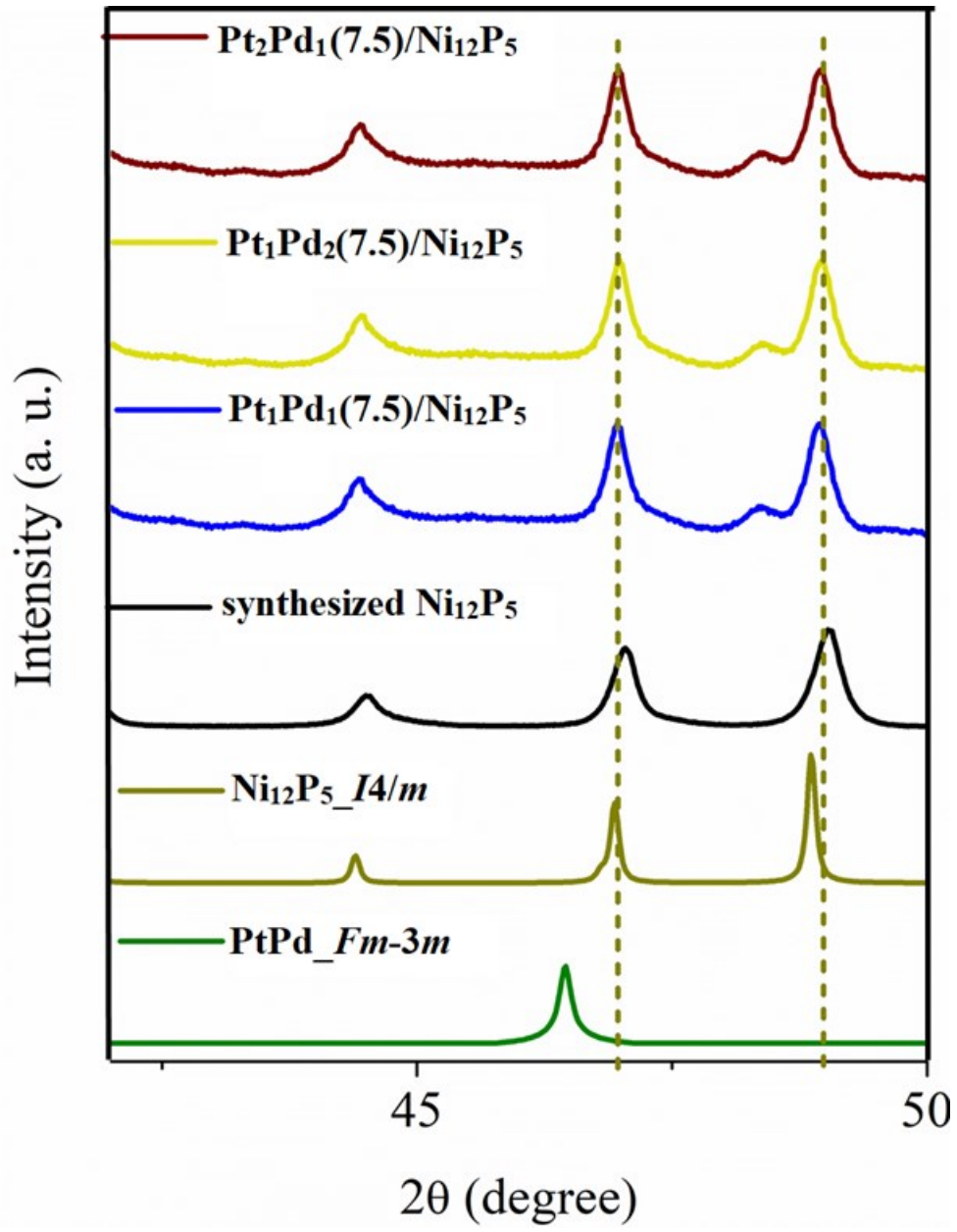


**Figure S4.** Enlarged view of the comparison of the PXRD patterns of $Pt_1Pd_1(7.5)/Ni_{12}P_5$, $Pt_1Pd_2(7.5)/Ni_{12}P_5$ and $Pt_2Pd_1(7.5)/Ni_{12}P_5$ with simulated patterns of PtPd alloy and tetragonal phase of $Ni_{12}P_5$.

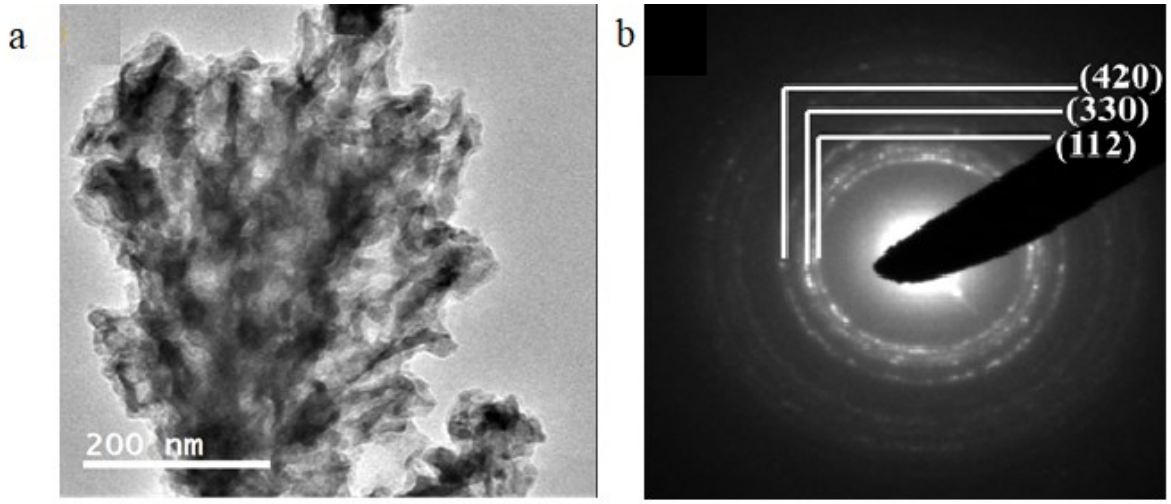


**Figure S5.** TEM images **(a)**and corresponding SAED pattern **(b)** of $Ni_{12}P_5$.

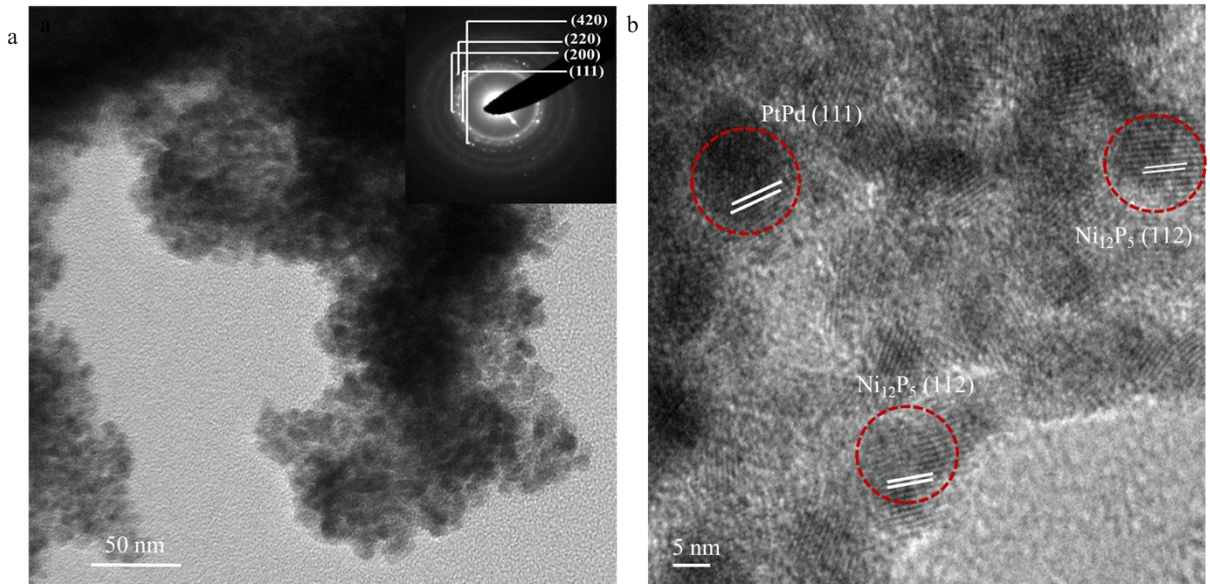


**Figure S6. (a)** TEM and (b) high resolution TEM image $Pt_1Pd_1(7.5)/Ni_{12}P_5$. Inset shows the corresponding SAED pattern of $Pt_1Pd_1(7.5)/Ni_{12}P_5$.

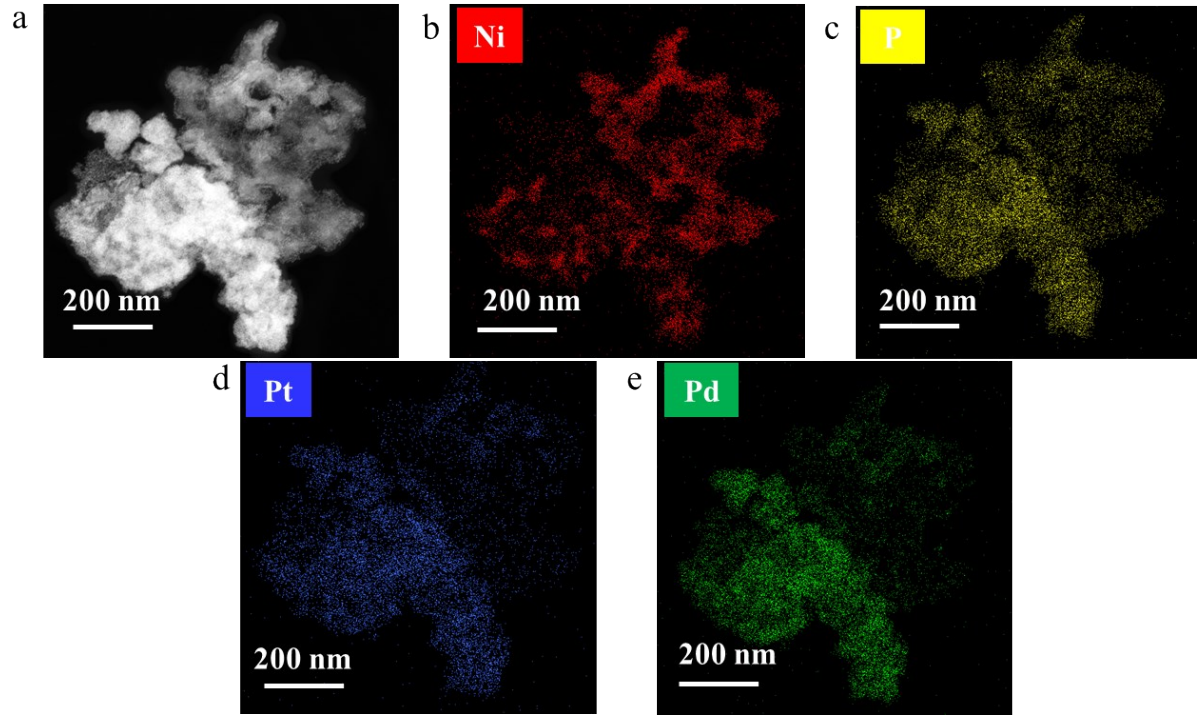


**Figure S7(a)** HAADF-STEM image of $Pt_1Pd_2(7.5)/Ni_{12}P_5$ and corresponding elemental mappings **(b)** Ni, **(c)** P, **(d)** Pt and **(e)** Pd.

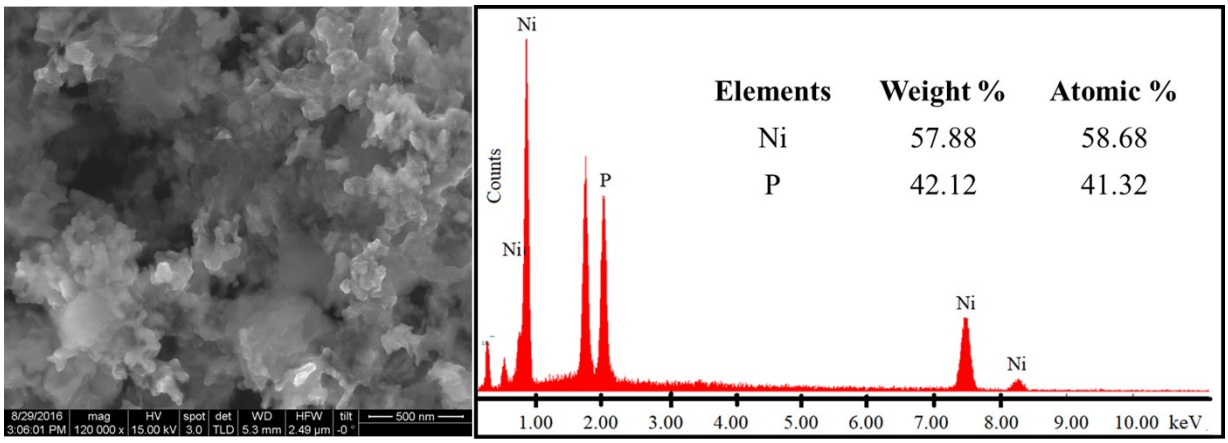


**Figure S8.** FESEM image and EDS spectrum (inset table represents elemental composition) of $Ni_{12}P_5$ nanoparticles.

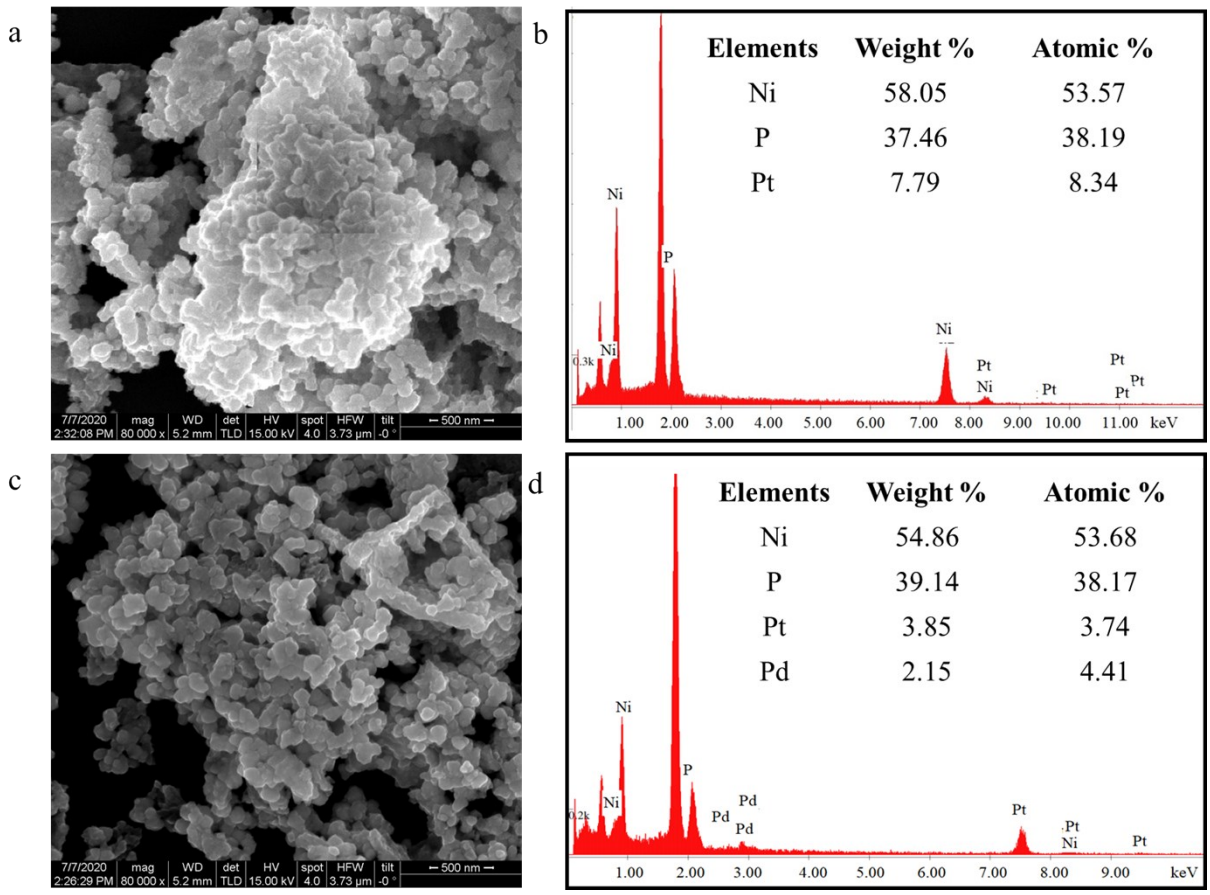


**Figure S9.** FESEM image and EDS spectrum (inset table represents elemental composition) of $Pt/Ni_{12}P_5$ (**a**, **b**) and $Pt_1Pd_1(5)/Ni_{12}P_5$ (**c**, **d**) nanoparticles.

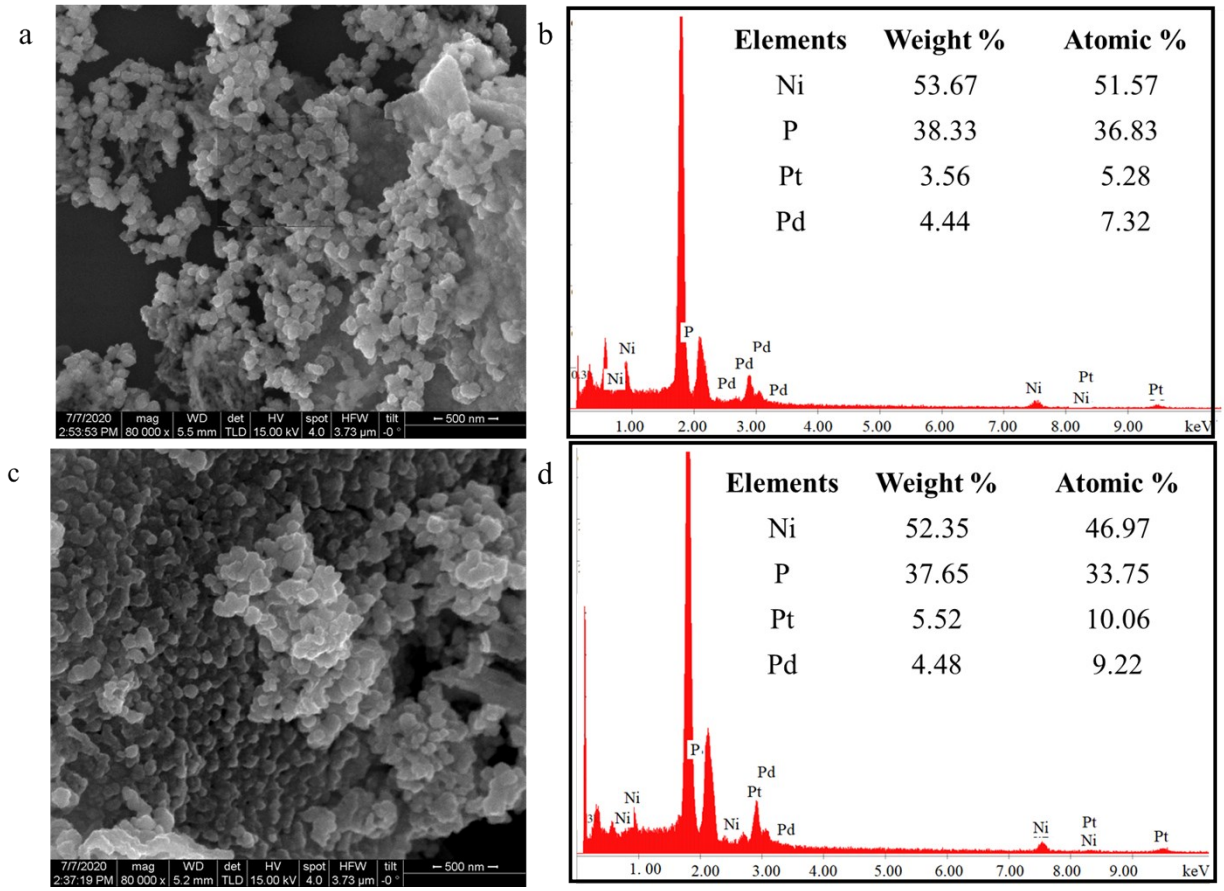


**Figure S10.** FESEM image and EDS spectrum (inset table represents elemental composition) of $Pt_1Pd_1(7.5)/Ni_{12}P_5$ (10) (**a**, **b**) and $Pt_1Pd_1(10)/Ni_{12}P_5$ (**c**, **d**) nanoparticles.

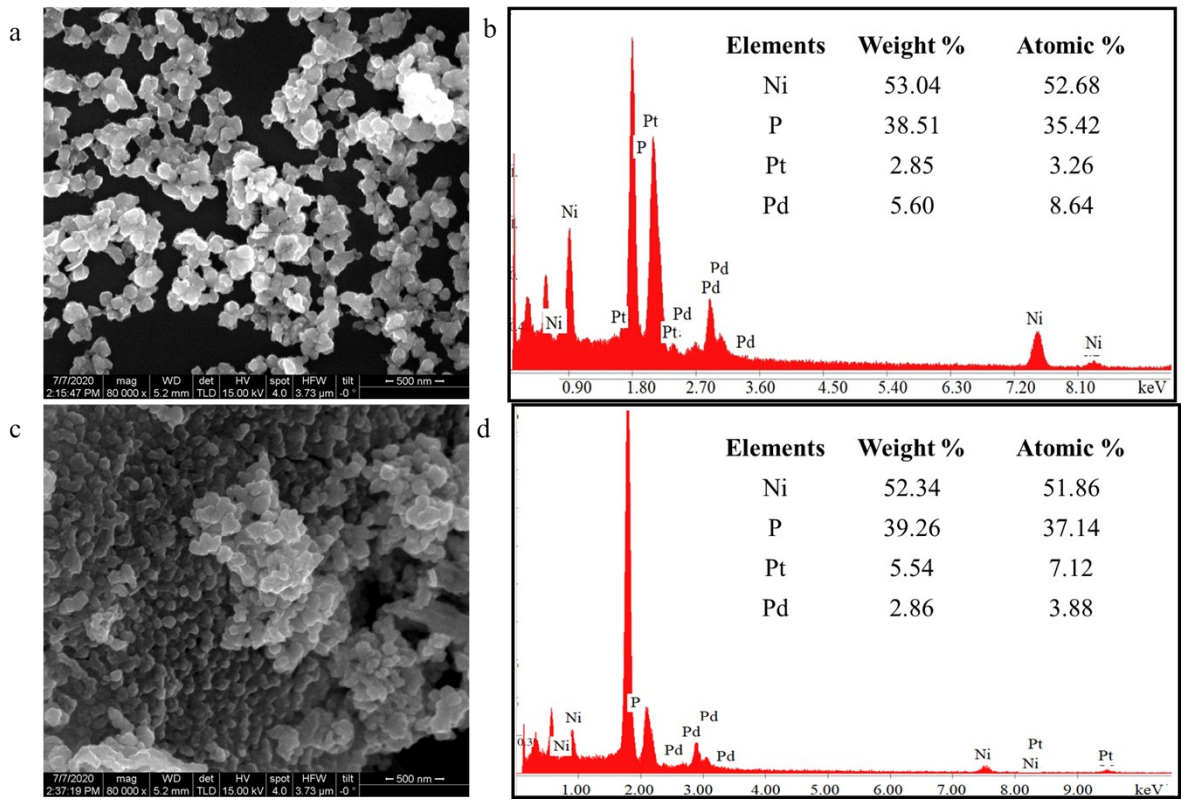


**Figure S11.** FESEM image andEDS spectrum (inset table represents elemental composition) of $Pt_1Pd_2(7.5)/Ni_{12}P_5$ (**a**, **b**) and $Pt_2Pd_1(7.5)/Ni_{12}P_5$ (**c**, **d**) nanoparticles.

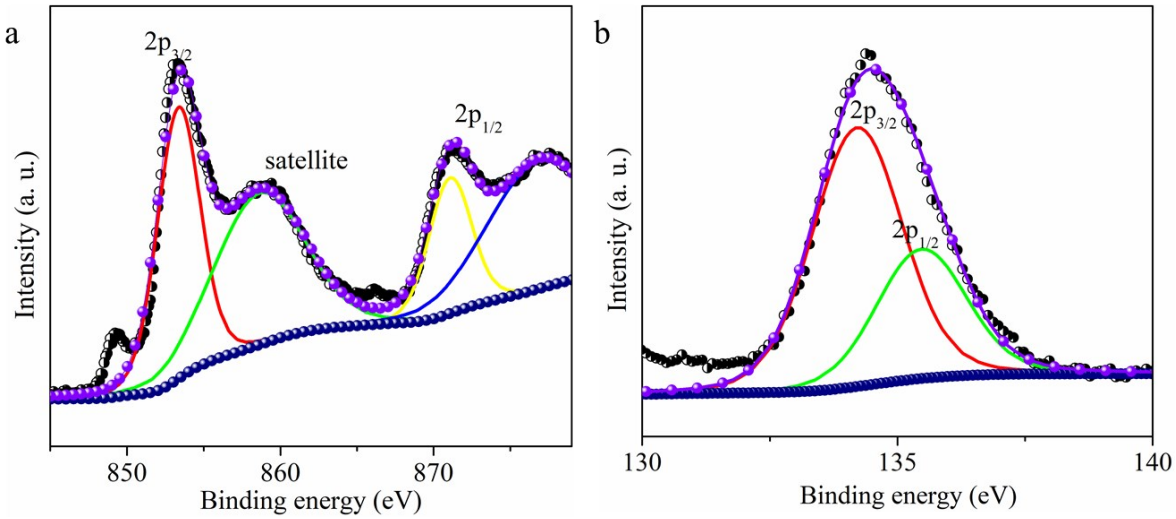


**Figure S12.** XPS spectra of Ni $2p_{3/2}$**(a)** and P $2p_{3/2}$**(b)** in bare $Ni_{12}P_5$. The red and yellow peak in (a) denotes the area under Ni $2p_{3/2}$ and $2p_{1/2}$ whereas the green and blue represents area under Ni 2p satellite peaks. The P $2p_{3/2}$ and $2p_{1/2}$ peaks are represented by red and green curves respectively in (b).

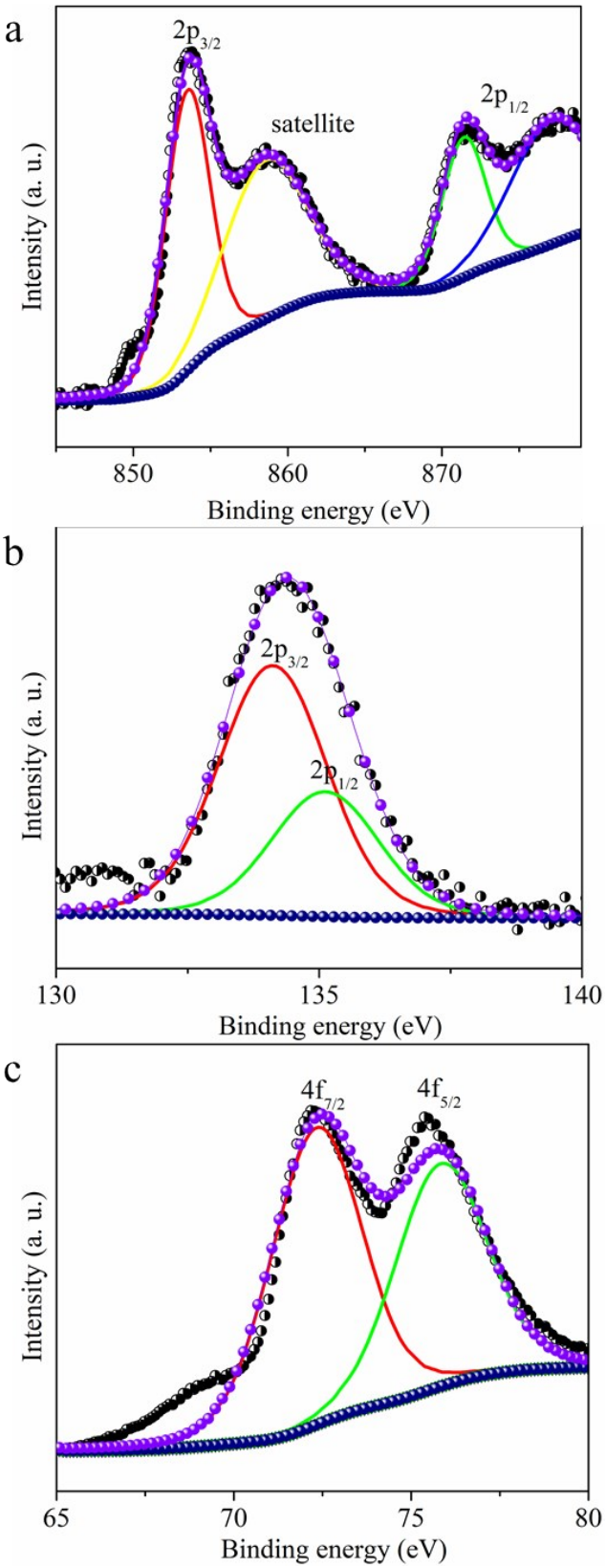


**Figure S13.** XPS spectra of Ni 2p **(a)**, P 2p **(b)**and Pt 4f**(c)** in $Pt/Ni_{12}P_5$. The red and yellow peak in **(a)** denotes the area under Ni $2p_{3/2}$ and $2p_{1/2}$ whereas the green and blue represents area under Ni 2p satellite peaks. The P $2p_{3/2}$ and $2p_{1/2}$ peaks are represented by red and

green curves respectively in **(b)**. Green and yellow curves in **(c)** denotes the area under curve due to Pt $4f_{7/2}$ and $4f_{5/2}$ respectively.

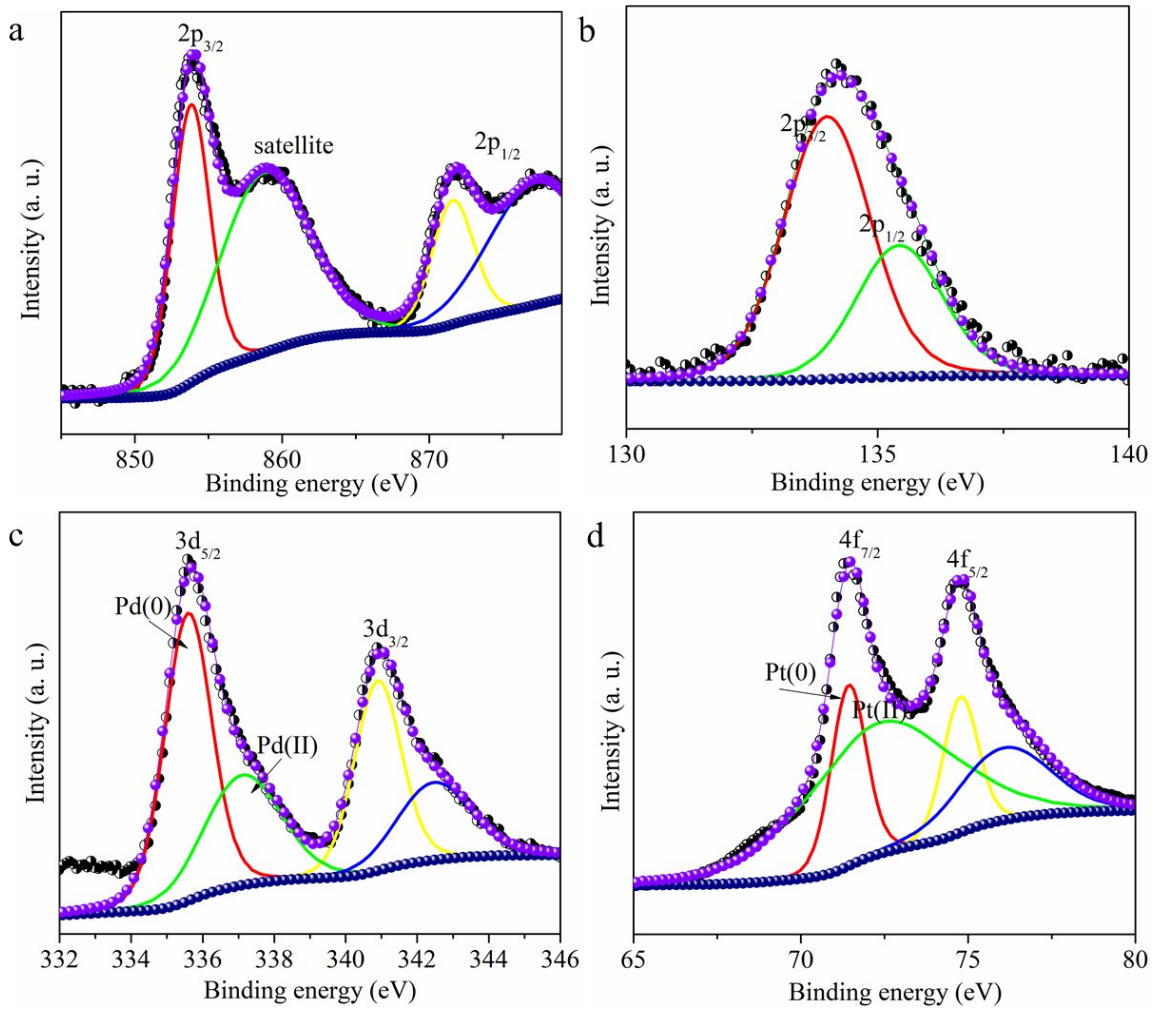


**Figure S14.** XPS spectra of Ni 2p **(a)**, P 2p **(b)**, Pd 3d **(c)** and Pt 4f**(d)** in $Pt_1Pd_1(5)/Ni_{12}P_5$. The red and yellow peak in **(a)** denotes the area under Ni $2p_{3/2}$ and $2p_{1/2}$ whereas the green and blue represents area under Ni 2p satellite peaks. The P $2p_{3/2}$ and $2p_{1/2}$ peaks are represented by red and green curves respectively in **(b)**. Pd $3d_{5/2}$ and $3d_{3/2}$ are represented by the red and yellow curves and green and blue curves shows the presence of Pd(II) from PdO species in **(c)**. Red and yellow curves in **(d)** denotes the area under curve due to Pt $4f_{7/2}$ and $4f_{5/2}$ respectively whereas the green curve shows the presence of Pt(II) from PtO.

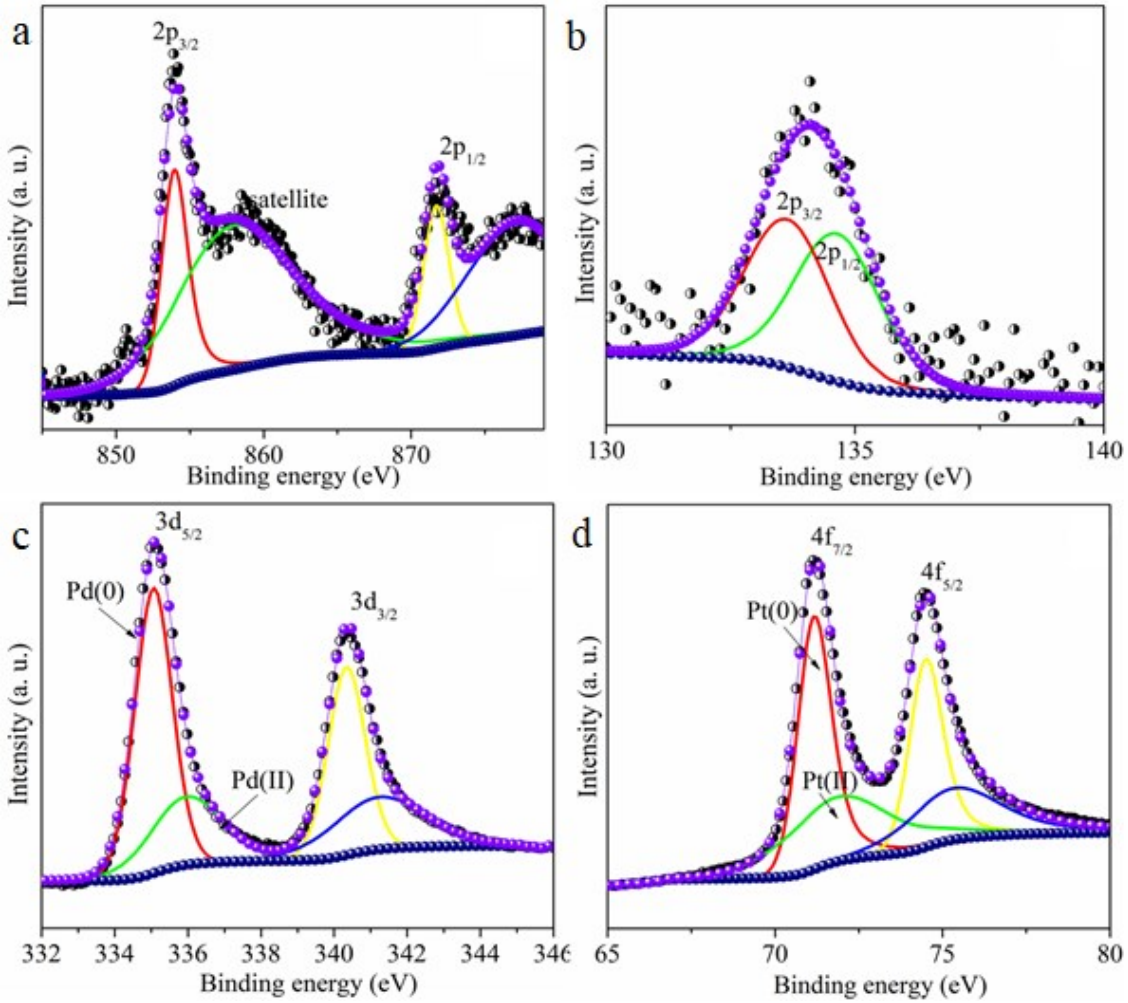


**Figure S15.** XPS spectra of Ni 2p **(a)**, P 2p **(b)**, Pd 3d **(c)** and Pt 4f**(d)** in $Pt_1Pd_1(7.5)/Ni_{12}P_5$. The red and yellow peak in **(a)** denotes the area under $Ni2p_{3/2}$ and $2p_{1/2}$ whereas the green and blue represents area under Ni 2p satellite peaks. The P $2p_{3/2}$ and $2p_{1/2}$ peaks are represented by red and green curves respectively in **(b)**. Pd $3d_{5/2}$ and $3d_{3/2}$ are represented by the red and yellow curves and green and blue curves shows the presence of Pd(II) from PdO species in **(c)**. Red and yellow curves in **(d)** denotes the area under curve due to Pt $4f_{7/2}$ and $4f_{5/2}$ respectively whereas the green curve shows the presence of Pt(II) from PtO.

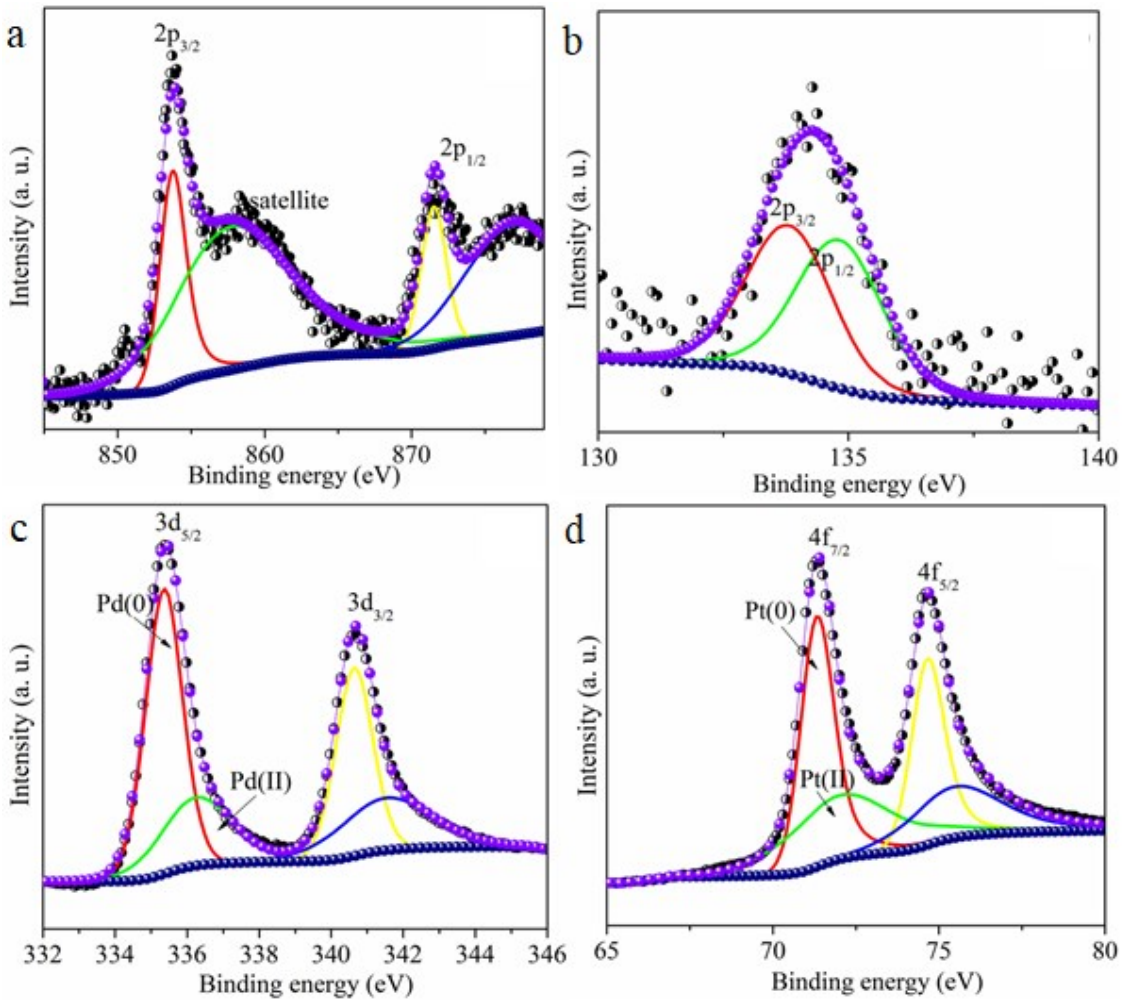


**Figure S16.** XPS spectra of Ni 2p **(a)**, P 2p **(b)**, Pd 3d **(c)** and Pt 4f**(d)** in $Pt_1Pd_2(7.5)/Ni_{12}P_5$. The red and yellow peak in **(a)** denotes the area under Ni $2p_{3/2}$ and $2p_{1/2}$ whereas the green and blue represents area under Ni 2p satellite peaks. The P $2p_{3/2}$ and $2p_{1/2}$ peaks are represented by red and green curves respectively in **(b)**. Pd $3d_{5/2}$ and $3d_{3/2}$ are represented by the red and yellow curves and green and blue curves shows the presence of Pd(II) from PdO species in **(c)**. Red and yellow curves in **(d)** denotes the area under curve due to Pt $4f_{7/2}$ and $4f_{5/2}$ respectively whereas the green curve shows the presence of Pt(II) from PtO.

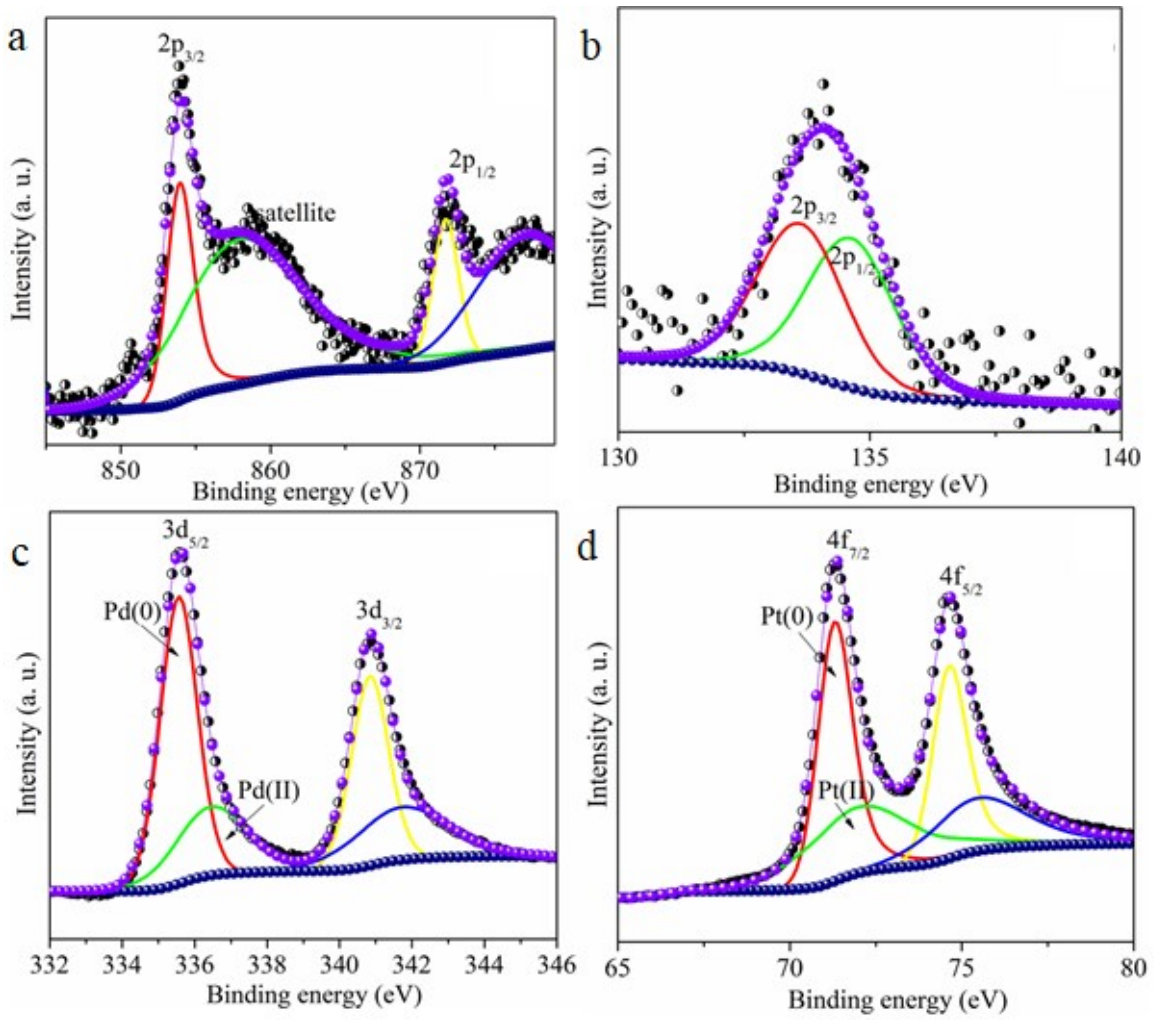


**Figure S17.** XPS spectra of Ni 2p**(a)**, P 2p**(b)**, Pd 3d **(c)** and Pt 4f **(d)** $Pt_2Pd_1(7.5)/Ni_{12}P_5$. The red and yellow peak in **(a)** denotes the area under $Ni2p_{3/2}$ and $2p_{1/2}$ whereas the green and blue represents area under Ni 2p satellite peaks. The P $2p_{3/2}$ and $2p_{1/2}$ peaks are represented by red and green curves respectively in **(b)**. Pd $3d_{5/2}$ and $3d_{3/2}$ are represented by the red and yellow curves and green and blue curves shows the presence of Pd(II) from PdO species in **(c)**. Red and yellow curves in **(d)** denotes the area under curve due to Pt $4f_{7/2}$ and $4f_{5/2}$ respectively whereas the green curve shows the presence of Pt(II) from PtO.

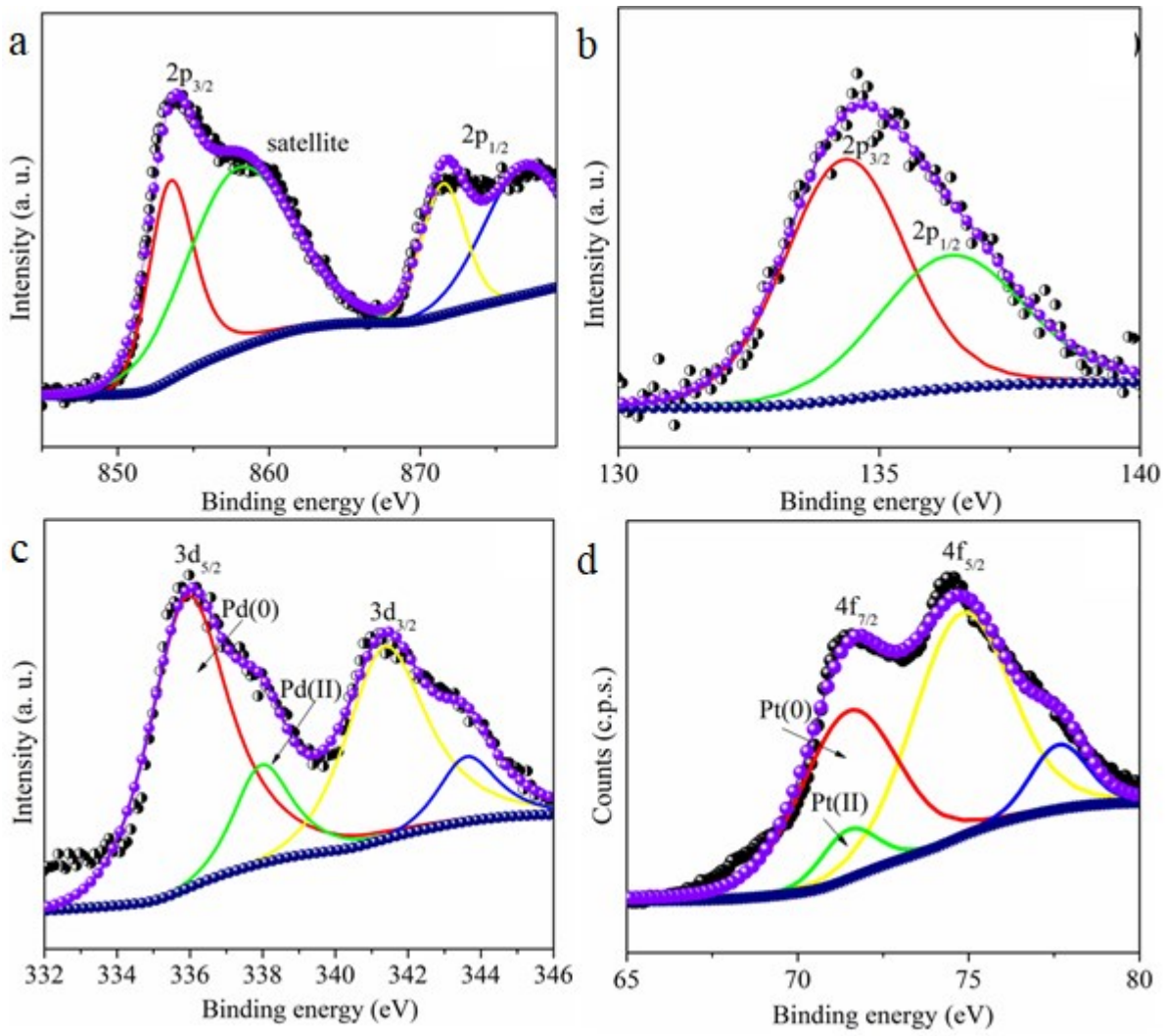


**Figure S18.** XPS spectra of Ni 2p **(a)**, P 2p **(b)**, Pd 3d **(c)** and Pt 4f **(d)** in $Pt_1Pd_1(10)/Ni_{12}P_5$ (10). The red and yellow peak in **(a)** denotes the area under Ni $2p_{3/2}$ and $2p_{1/2}$ whereas the green and blue represents area under Ni 2p satellite peaks. The P $2p_{3/2}$ and $2p_{1/2}$ peaks are represented by red and green curves respectively in **(b)**. Pd $3d_{5/2}$ and $3d_{3/2}$ are represented by the red and yellow curves and green and blue curves shows the presence of Pd(II) from PdO species in **(c)**. Red and yellow curves in **(d)** denotes the area under curve due to Pt $4f_{7/2}$ and $4f_{5/2}$ respectively whereas the green curve shows the presence of Pt(II) from PtO.

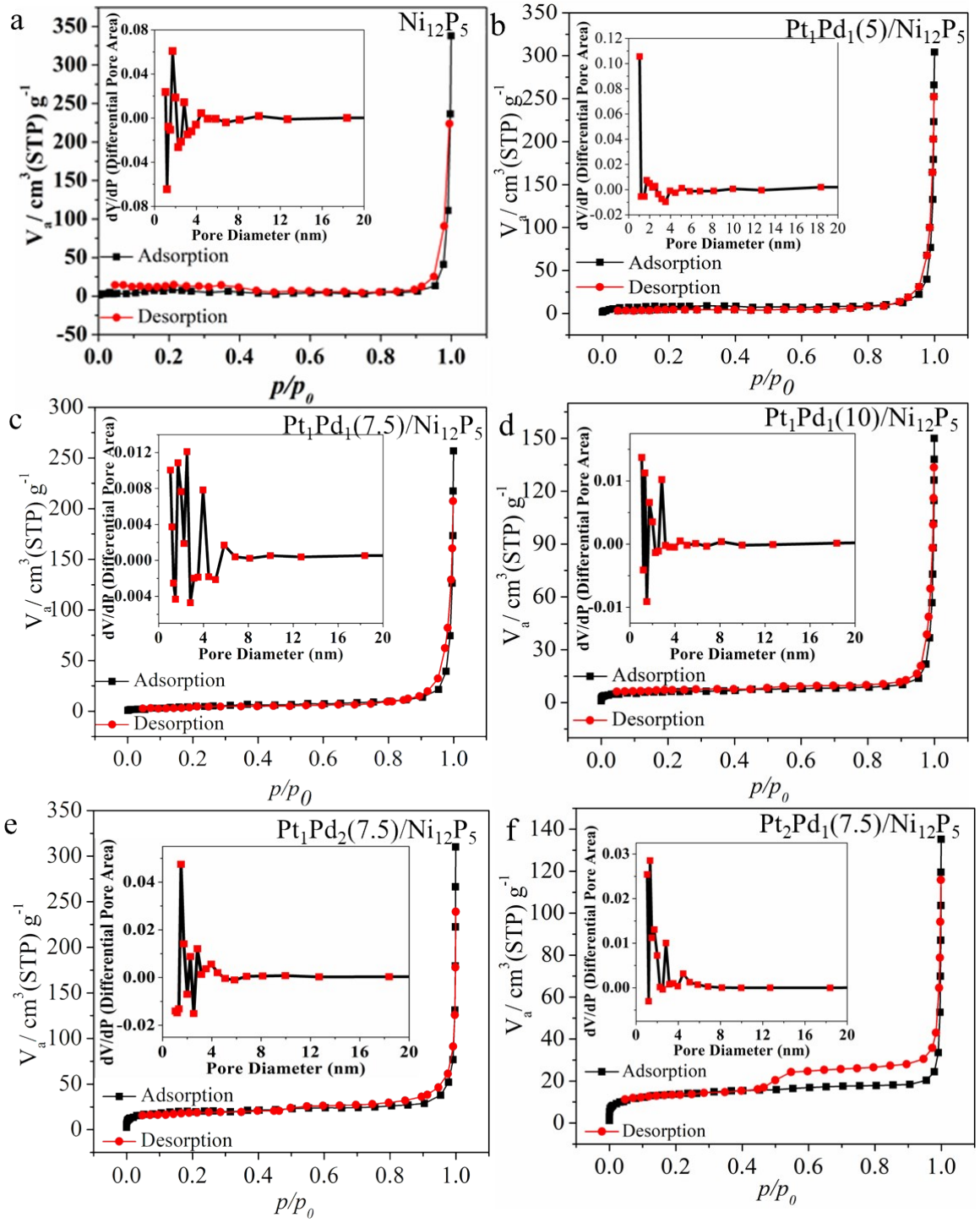


**Figure S19**. $N_2$ adsorption/desorption isotherm of the various synthesized catalysts. Figure inset shows the pore size distribution. The Brunauer-Emmett-Teller (BET) equation was used tocalculate the specific surface area. Pore size distributions were obtained using the Barrett-Joyner-Halenda (BJH) method from the adsorption branch of the isotherm

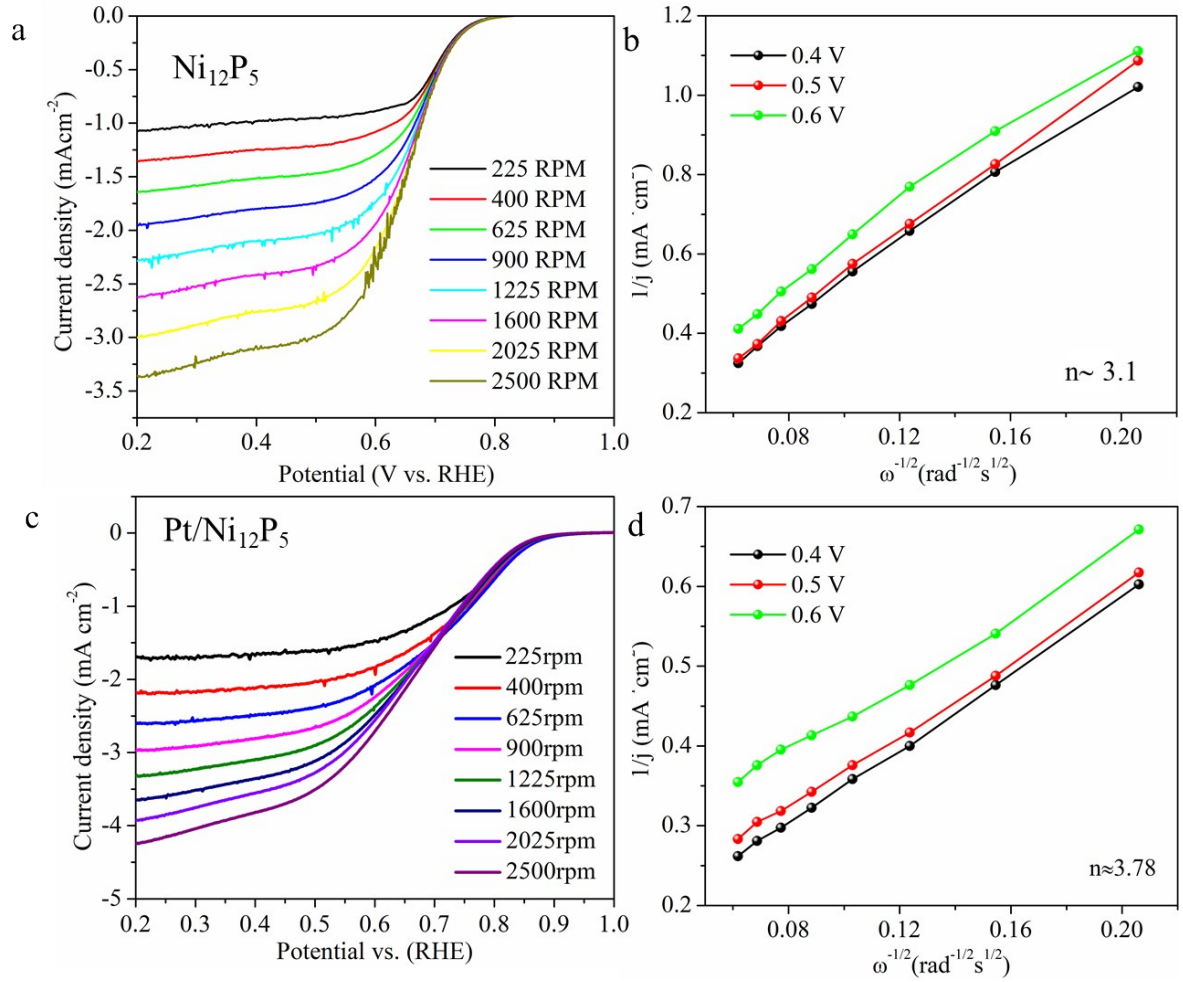


**Figure S20**. ORR LSV curves in 0.1 M KOH v RHE (**a** and **c**) and (**b** and **d**) K-L plots of the electrocatalysts exhibiting varying slopes corresponding to different electron reduction processes in the working potential range between 0.4-0.8V of $Ni_{12}P_5$ and $Pt/Ni_{12}P_5$ respectively.

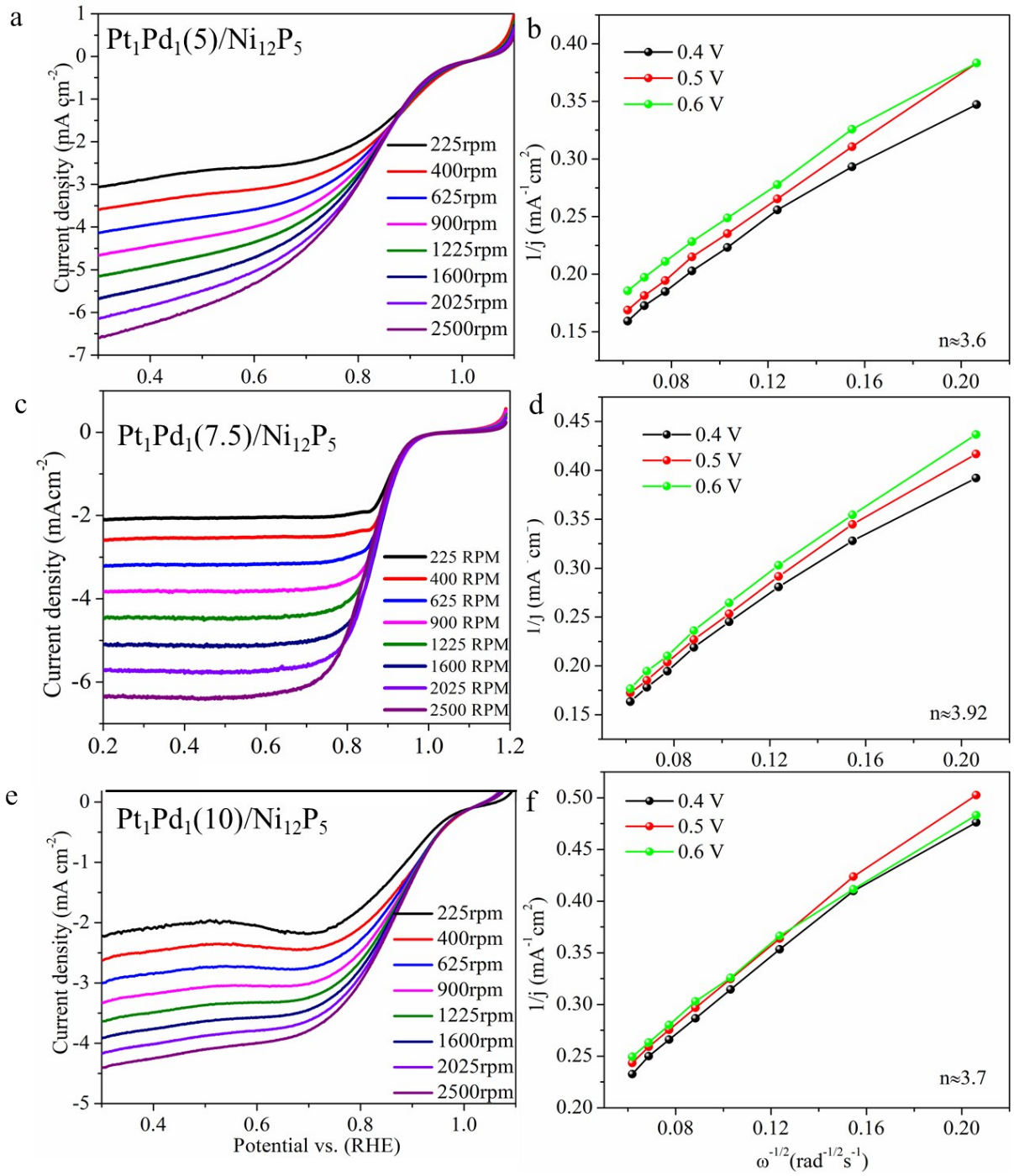


**Figure S21**. ORR LSV curves in 0.1 M KOH v RHE (**a** and **c**) and (**b** and **d**) K-L plots of the electrocatalysts exhibiting varying slopes corresponding to different electron reduction processes in the working potential range between 0.4-0.8V of $Ni_{12}P_5$ and $Pt_1Pd_1(5)/Ni_{12}P_5$, $Pt_1Pd_1(7.5)/Ni_{12}P_5$ and $Pt_1Pd_1(10)/Ni_{12}P_5$ respectively.

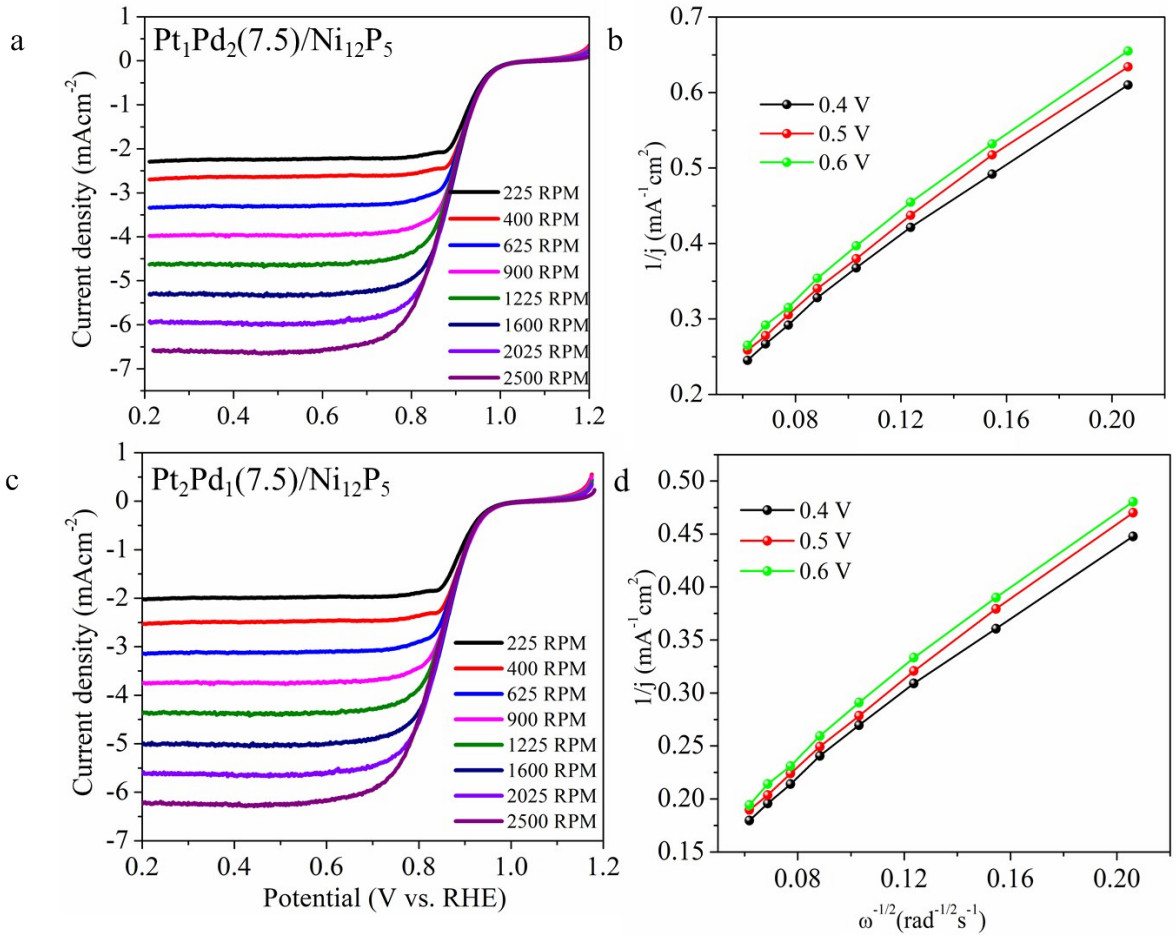


**Figure S22**. ORR LSV curves in 0.1 M KOH v RHE (**a** and **c**) and (**b** and **d**) K-L plots of the electrocatalysts exhibiting varying slopes corresponding to different electron reduction processes in the working potential range between 0.4-0.8V of $Pt_1Pd_2/Ni_{12}P_5$ and $Pt_2Pd_1(7.5)/Ni_{12}P_5$ catalysts respectively.

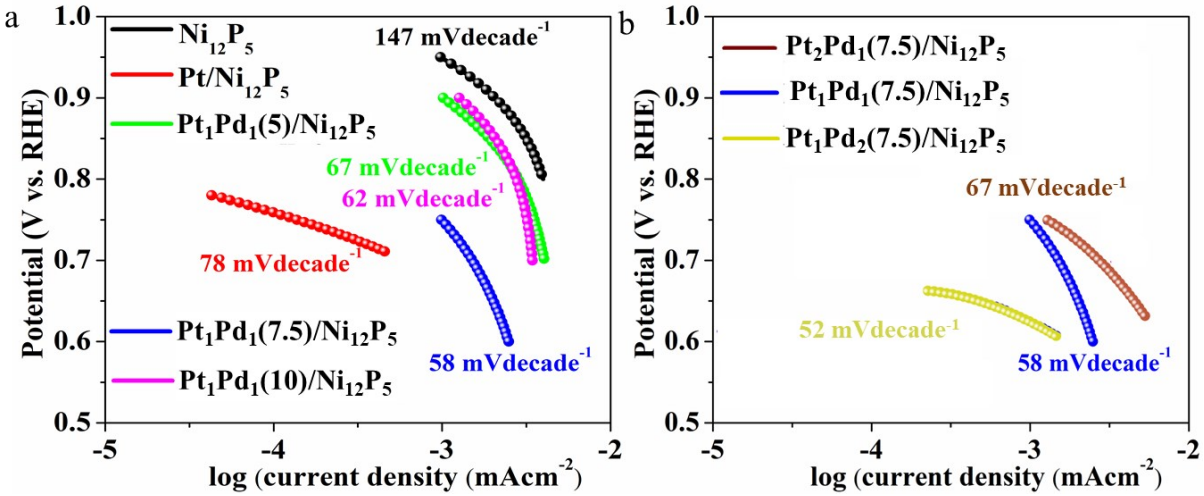


**Figure S23.** Tafel plots of $Ni_{12}P_5$, $Pt/Ni_{12}P_5$, $Pt_1Pd_1(5)/Ni_{12}P_5$, $Pt_1Pd_1(7.5)/Ni_{12}P_5$ and $Pt_1Pd_1(10)/Ni_{12}P_5$ (**a**) and $Pt_1Pd_1(7.5)/Ni_{12}P_5$, $Pt_1Pd_2(7.5)/Ni_{12}P_5$ and $Pt_2Pd_1(7.5)Ni_{12}P_5$ catalysts in 0.1M KOH.

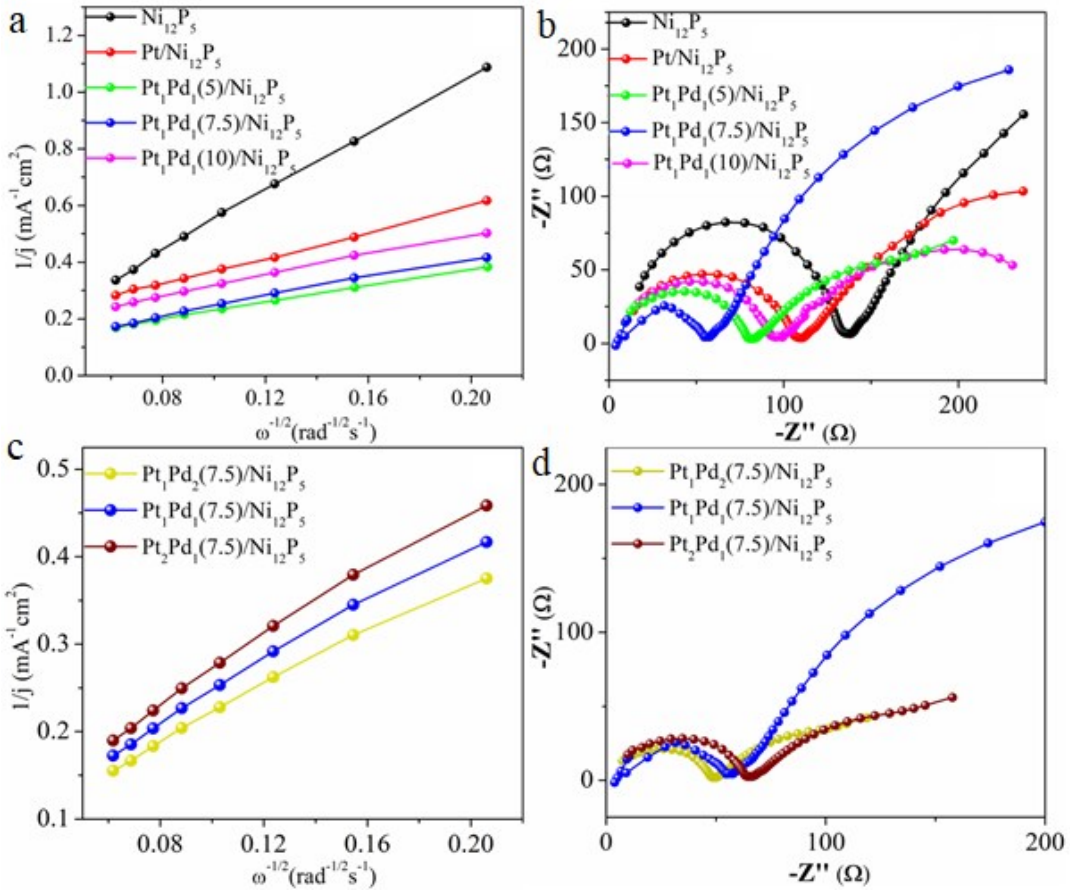


**Figure S24.** K-L plots of the electrocatalysts exhibiting varying slopes corresponding to different electron reduction processes (**a** and **c**), (**b** and **d**) Nyquist plots of the at $E_{1/2}$ showing the difference in $R_{CT}$ values across all the catalysts for ORR in 0.1M KOH**.**

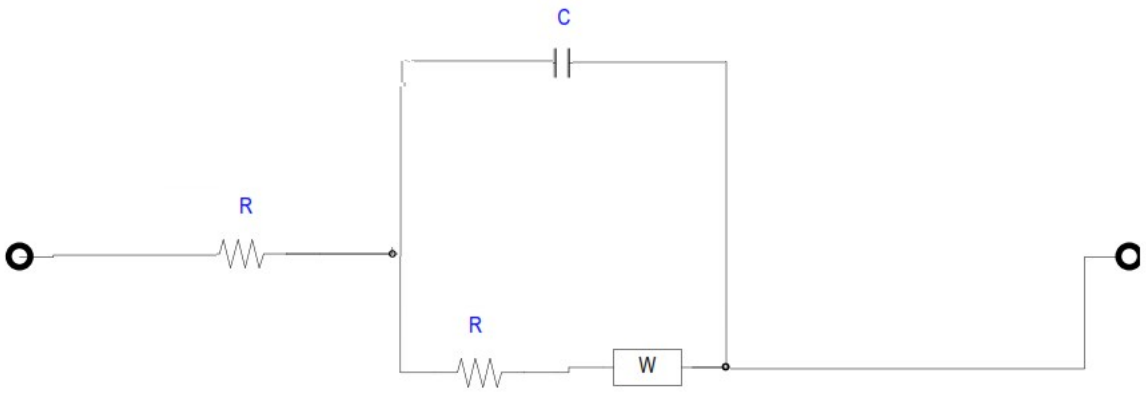


**Figure S25.** Equivalent circuit used for fitting the EIS spectra as seen in Figures S24b and S24d.

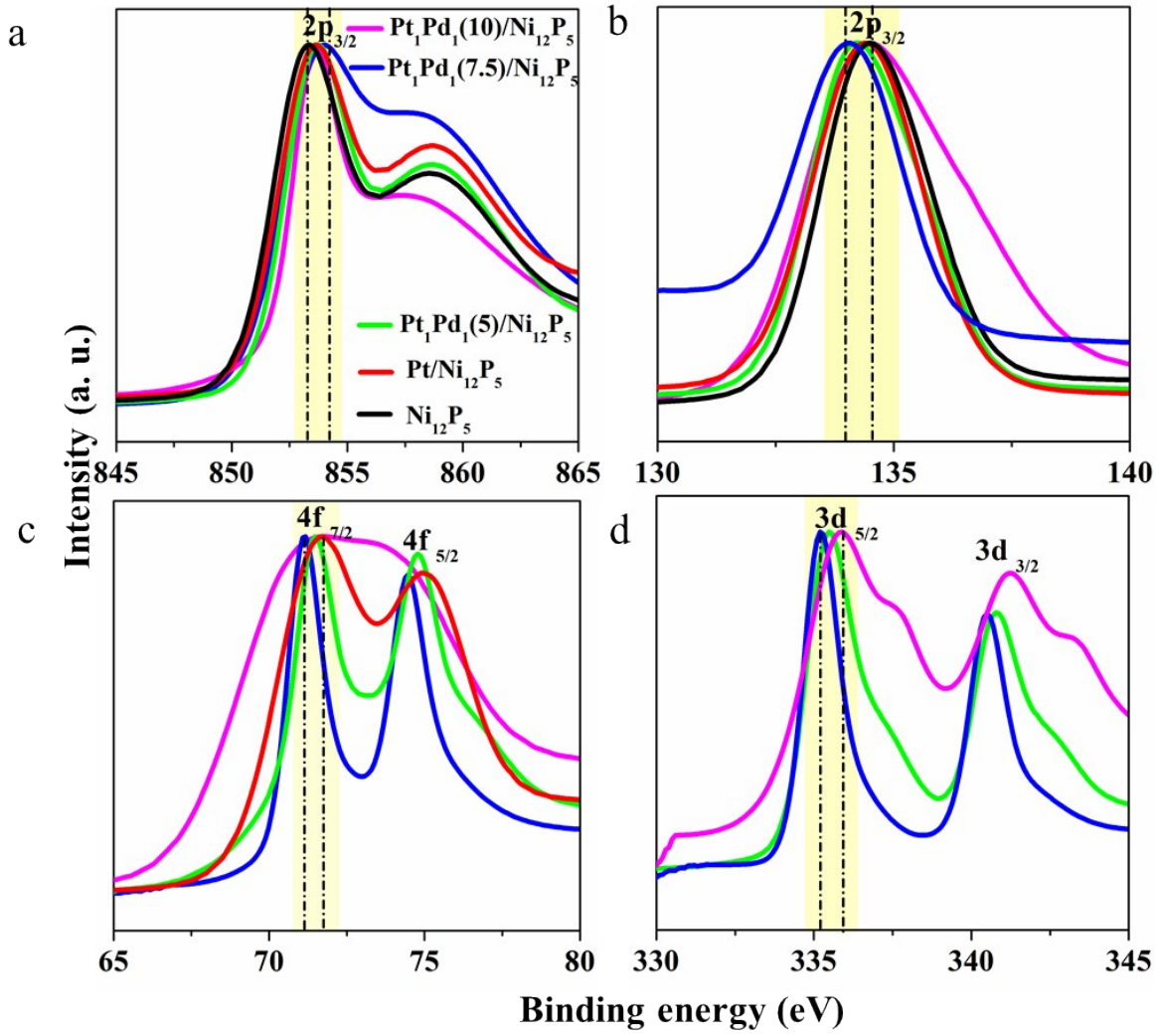


**Figure S26.** XPS binding energy shift of Ni $2p_{3/2}$ **(a)** P $2p_{3/2}$ **(b)** Pt $4f_{7/2}$ **(c)** and Pd $3d_{5/2}$ **(d)** in $Ni_{12}P_5$, $Pt/Ni_{12}P_5$, $Pt_1Pd_1(5)/Ni_{12}P_5$ $Pt_1Pd_1(7.5)/Ni_{12}P_5$ and $Pt_1Pd_1(10)/Ni_{12}P_5$.

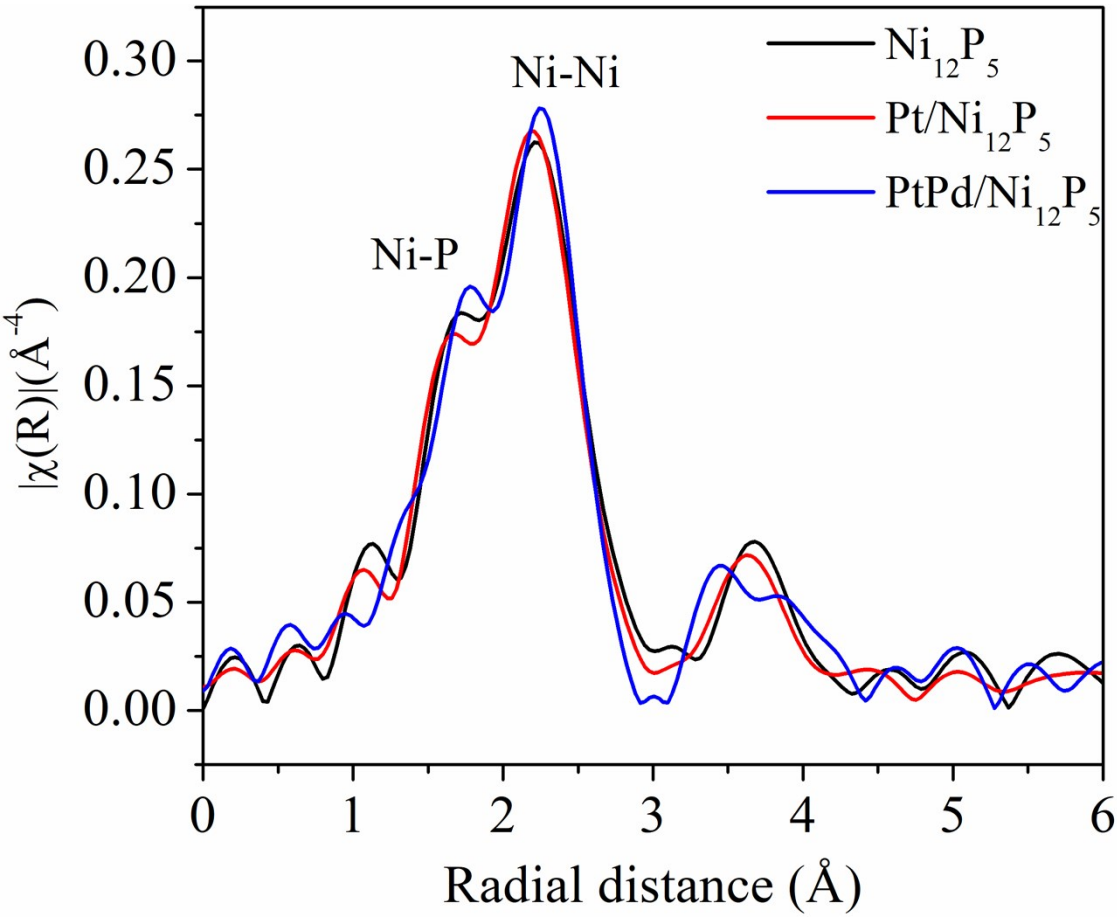


**Figure S27.** Fourier transform magnitudes of the Ni K-edge EXAFS oscillations in $Ni_{12}P_5$, $Pt/Ni_{12}P_5$ and $PtPd/Ni_{12}P_5$.

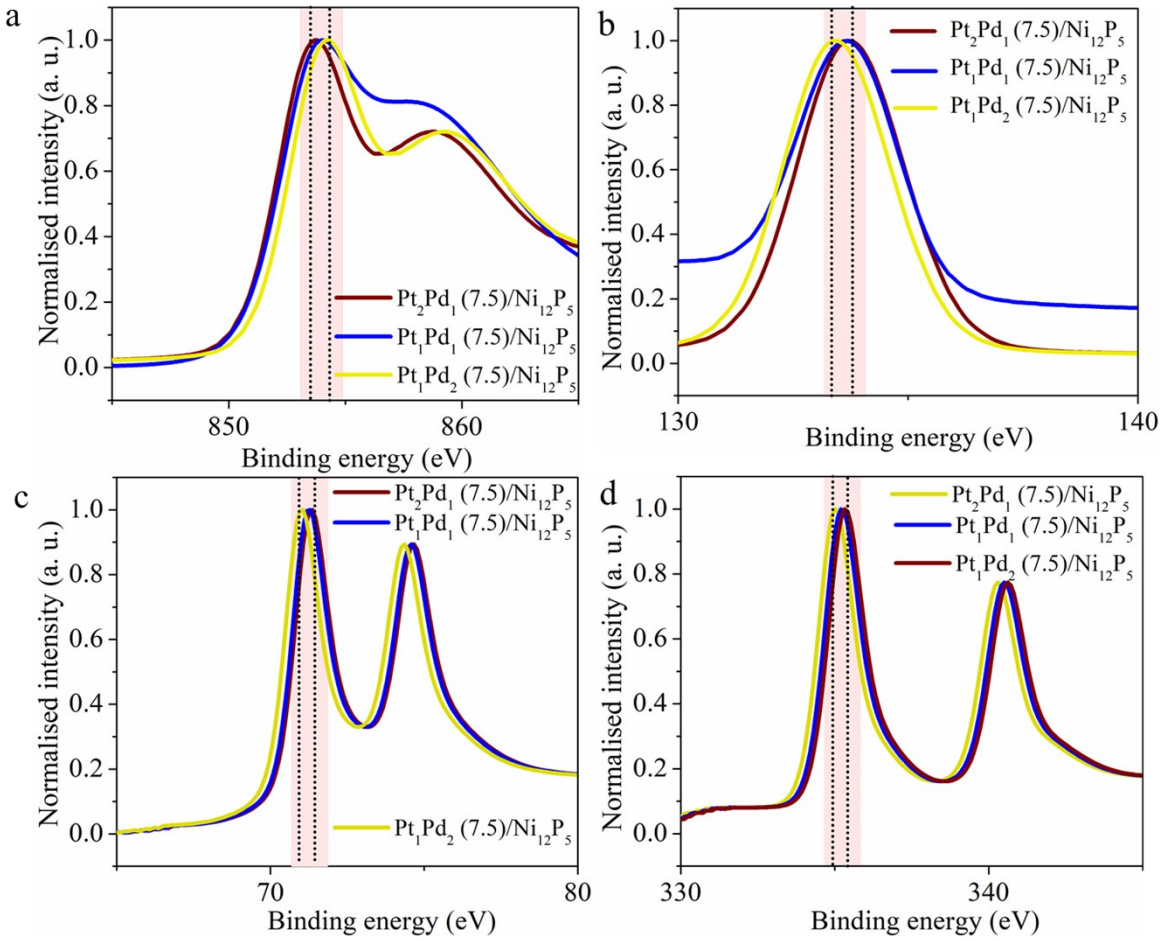


**Figure S28.** XPS binding energy shift of Ni $2p_{3/2}$**(a)** P $2p_{3/2}$**(b)** Pt $4f_{7/2}$**(c)** and Pd $3d_{5/2}$**(d)** in $Pt_1Pd_1(7.5)/Ni_{12}P_5$, $Pt_1Pd_2(7.5)/Ni_{12}P_5$ and $Pt_2Pd_1(7.5)/Ni_{12}P_5$ electrocatalysts.

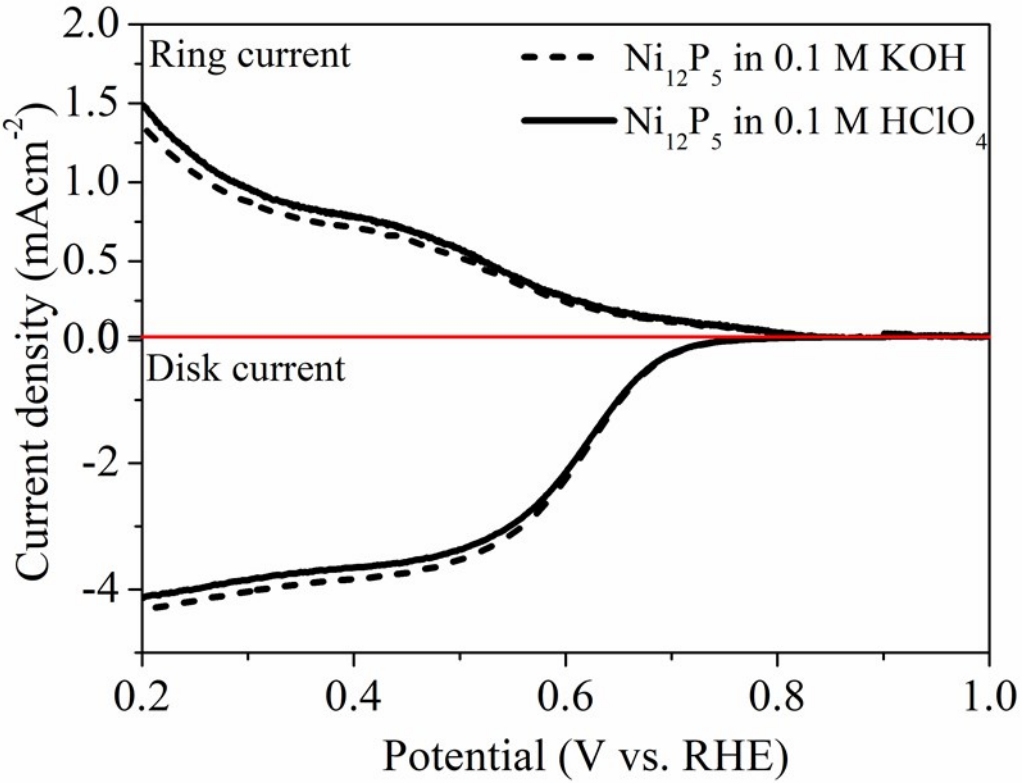


**Figure S29.** RRDE polarization curve of $Ni_{12}P_5$ recorded at 1600 RPM in $O_2$-saturated 0.1M KOH and 0.1M $HClO_4$.

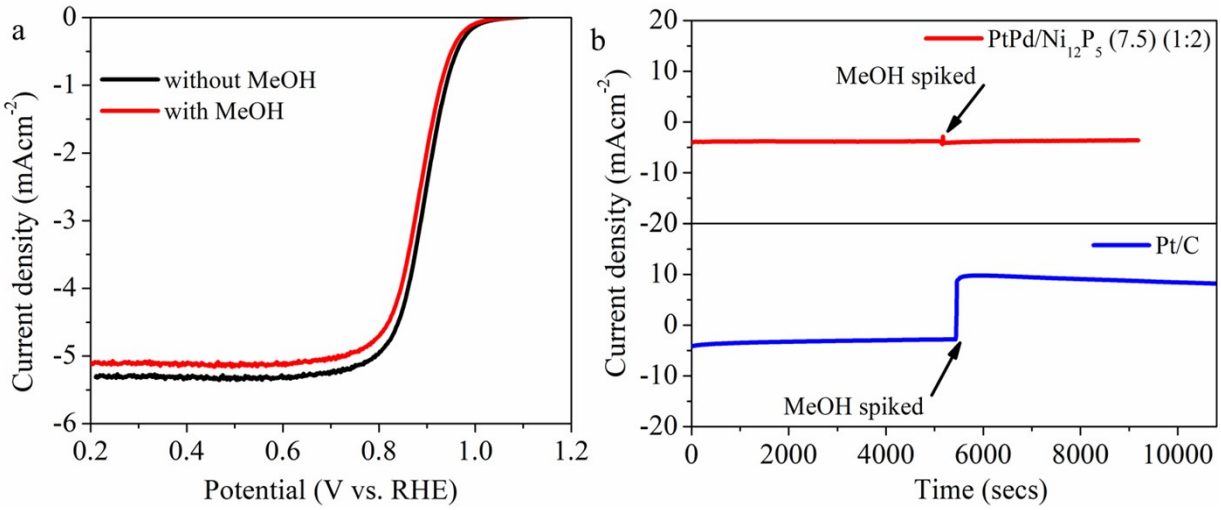


**Figure S30. (a)** LSVs before and after MeOH injection $Pt_1Pd_2(7.5)/Ni_{12}P_5$ and **(b)** comparative chronoamperometic curves with MeOH injection between Pt/C and $Pt_1Pd_2(7.5)/Ni_{12}P_5$.

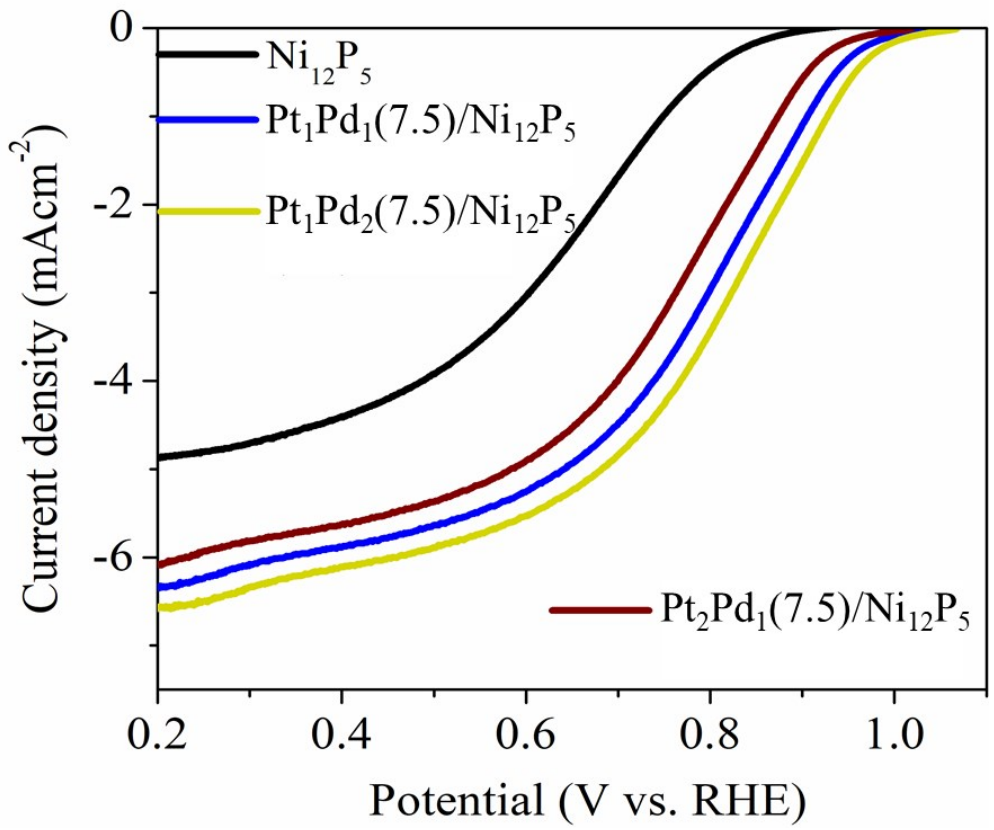


**Figure S31**. ORR LSV curves of different electrocatalysts in 0.1 M $HClO_4$ v RHE.

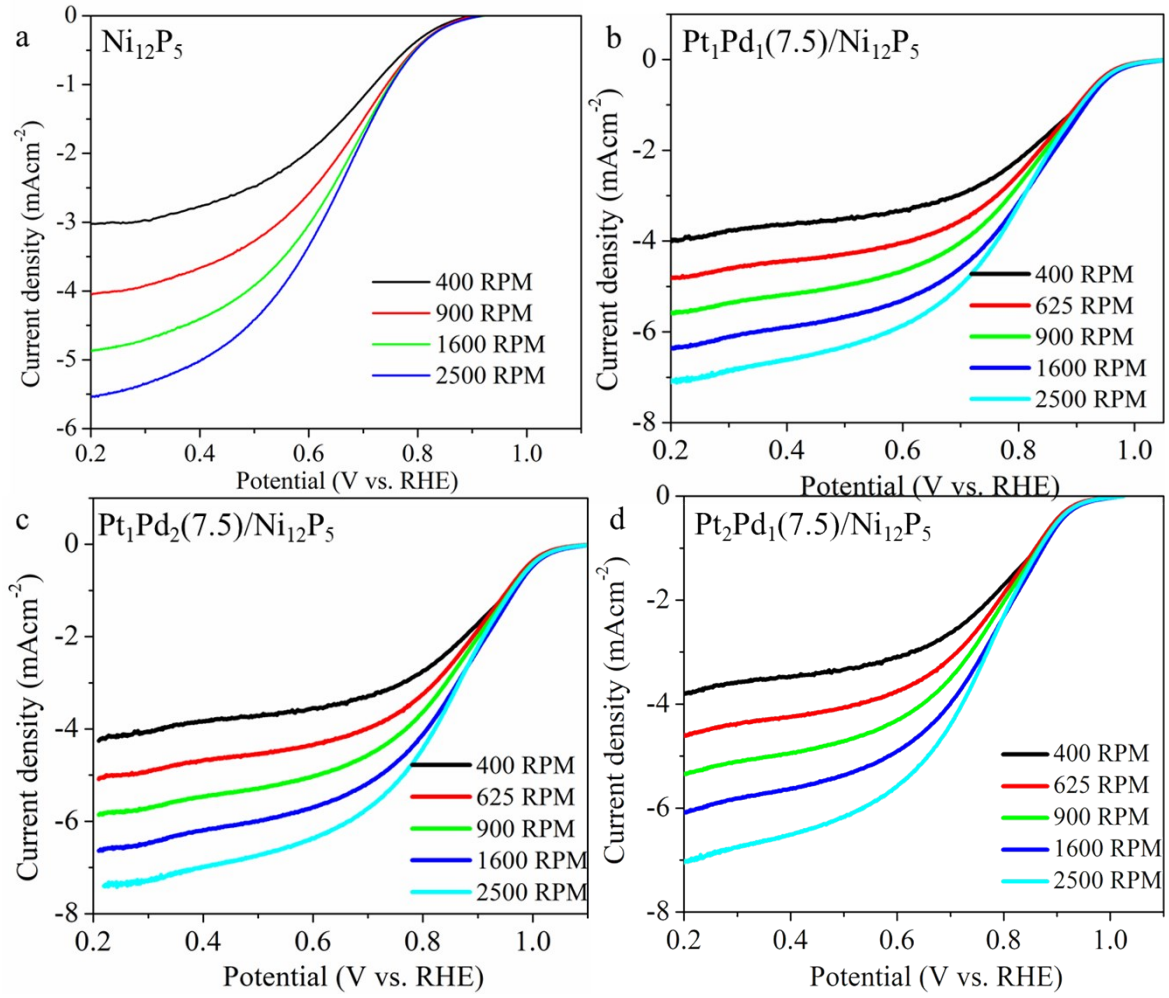


**Figure S32**. ORR LSV curves of in 0.1 M $HClO_4$ at different rotation rates for **(a)** $Ni_{12}P_5$ **(b)** $Pt_1Pd_1(7.5)/Ni_{12}P_5$, **(c)** $Pt_1Pd_2(7.5)/Ni_{12}P_5$ and **(d)** $Pt_2Pd_1(7.5)/Ni_{12}P_5$.

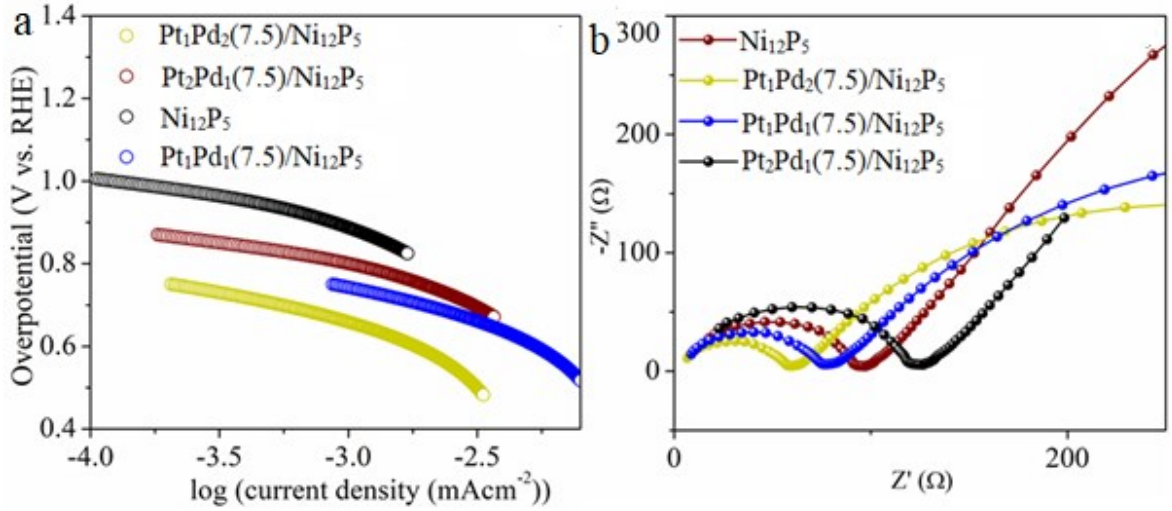


**Figure S33. (a)** Tafel slope and **(b)** Nyquist plots of the at $E_{1/2}$ showing the difference in $R_{CT}$ values across all the catalysts for ORR in 0.1M $HClO_4$.

**Figure S34.** Equivalent circuit used for fitting the EIS spectra obtained in figure S33.

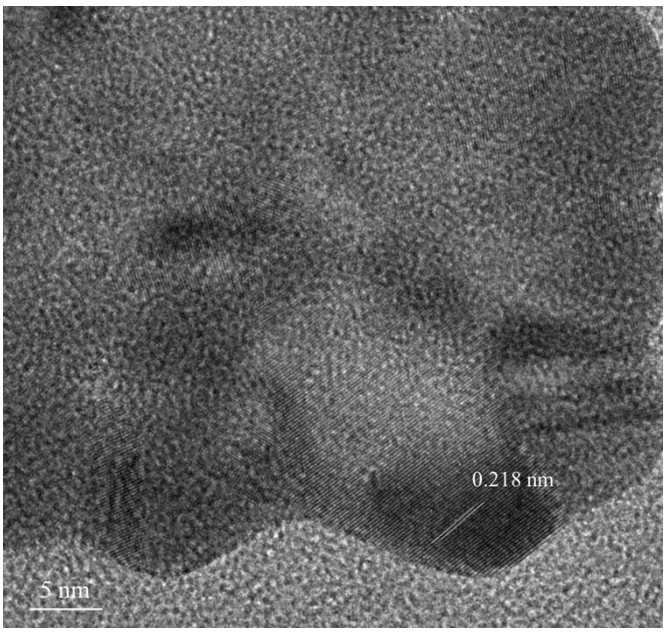


**Figure S35.** HRTEM of $Ni_{12}P_5$ after OER in 0.5 M KOH.

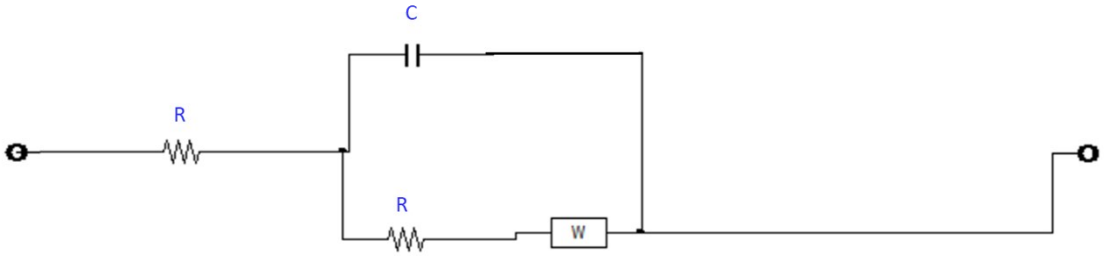


**Figure S36.** Equivalent circuit used for fitting the EIS spectra obtained in Figure 4b.

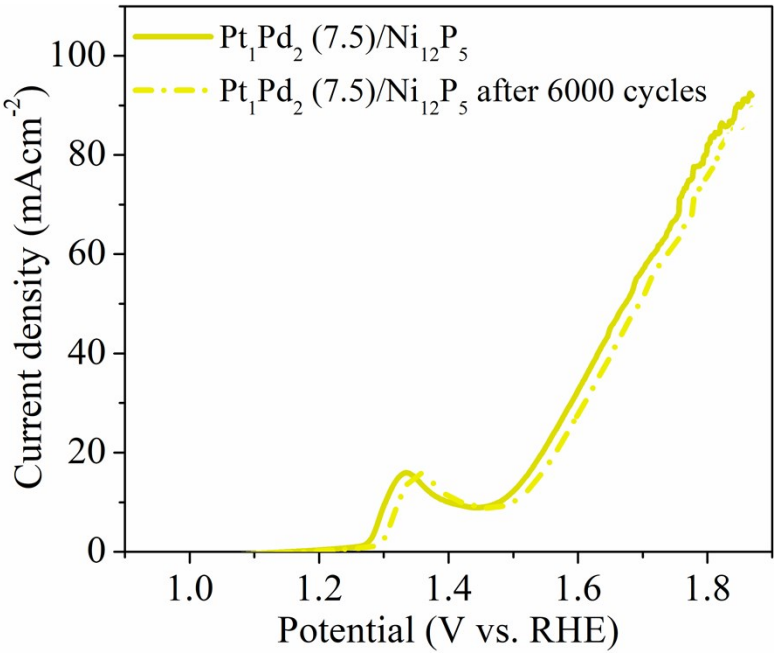


**Figure S37.** Comparison of LSV polarization curve for $Pt_1Pd_2$ (7.5)/$Ni_{12}P_5$ before and after potential cycling upto 6000 cycles after OER in 0.5 M KOH.

**Notes**

**S1:** As seen in **Figure S23,** $Ni_{12}P_5$ exhibits the highest Tafel slope value whereas $Pt_1Pd_2(7.5)/Ni_{12}P_5$ shows the lowest Tafel slope value of 52 mVdecade$^{-1}$ similar to the state-of-the-art Pt/C. All other PtPd/$Ni_{12}P_5$ catalysts exhibit slightly larger Tafel slope values which are still in consistent with the values of Pt based catalysts (**Figure S23**) and hence, can be inferred that all PtPd/$Ni_{12}P_5$ catalysts follow similar ORR mechanism. A comparison of the charge transfer resistances ($R_{CT}$) at $E_{1/2}$, from electrochemical impedance spectroscopic studies (**Figures S24b, S24d and S25**), reveals the facile charge transfer process in $Pt_1Pd_1(7.5)/Ni_{12}P_5$ as compared to the other catalysts due to reduced $R_{CT}$ values, indicating strong chemical coupling between PtPd and $Ni_{12}P_5$, which can contribute to the enhanced ORR activity. The EIS spectra show the presence of high and medium frequency arcs in the Nyquist plots ($R_e$ is Ohmic resistance and $R_{CT}$ is charge transfer resistance). The presence of a high frequency arc is attributed to the transport of oxygen intermediates within the electrode/electrolyte interface whereas the medium frequency arc in the other catalysts can be ascribed to atomic oxygen diffusion within the electrode followed by charge transfer. Since the medium frequency arc reduces it may stipulate the increased resistance related to oxygen diffusion at the electrode surface with optimum metal loading. The low frequency region corresponds to Warburg impedance ($Z_w$). As seen from **Table S2,** $Pt_1Pd_1(7.5)/Ni_{12}P_5$ exhibits the lowest $R_{CT}$ in terms of metal loading whereas variation in Pt:Pd ratio in $Pt_1Pd_1(7.5)/Ni_{12}P_5$ led to a further reduction of $R_{CT}$ value in $Pt_1Pd_2(7.5)/Ni_{12}P_5$ and an improvement in the overpotential close to the state-of-the-art Pt/C. Lower values of $R_e$, $R_{CT}$ and diffusion coefficient (D) can be attributed to enhanced conductivity upon metal loading which lowers the internal resistance and elevates charge-transfer kinetics.

**S2:** Pt/$Ni_{12}P_5$ showed a negative shift of Pt 4f peak by 0.1 eV whereas that for $Pt_1Pd_1(7.5)/Ni_{12}P_5$ showed the highest negative shift by 0.4 eV. Correspondingly, highest enhancement of $Ni^{2+}$ can be proposed for $Pt_1Pd_1(7.5)/Ni_{12}P_5$ catalyst implying that $Ni_{12}P_5$ surface after loading with PtPd NPs is enriched with abundant positively charged nickel ions. This is due to the electron donation from $Ni_{12}P_5$ to Pt/PtPd, which induces a strong electronic interaction between Pt/PtPd and $Ni_{12}P_5$. Different amounts of total metal loading (Pt+Pd) on $Ni_{12}P_5$ causes downward shift of binding energy for Pt 4f and Pd 3d. This demonstrates that electron transfer occurs between Pd and Pt with Pt and Pd becoming electron-rich consequently. $Pt_1Pd_1(7.5)/Ni_{12}P_5$ shows the highest negative shift of 0.4 eV with respect to Pt (**Figure S26d**) and 0.3 eV (**Figure S26c**) with that of Pd in comparison to binding energy values of $Pt_1Pd_1(5)/Ni_{12}P_5$ and $Pt_1Pd_1(10)/Ni_{12}P_5$.

**S3:** Water or hydrogen peroxide are the expected major products for electrochemical ORR depending on whether a direct 4e$^-$ or an indirect 2e$^-$ transfer process is taking place. Four e$^-$ pathway is desirable to achieve high energy efficiency. In order to calculate the number of electrons involved in ORR of the catalysts under this study, the plot of 1/j vs angular velocity ($\omega^{-1/2}$) of the different electrocatalysts at different rotation rates between 0.4 to 0.7 V (**Figures S20-S22**) were fitted to the K-L equation at different potentials which yielded a series of parallel lines with a slope B. The linearity and parallel behaviour of K-L plots for the samples shows the uniformity of 4e$^-$ transfer pathway across the wide potential range (0.8–0.4 V) (**Table S1**). The comparison of K-L plots of all the catalysts (**Figures S24a** and **S24c)** shows that electron transfer number varies from 3.1 in $Ni_{12}P_5$ to 4 in PtPd deposited $Ni_{12}P_5$. RRDE measurements were further conducted to check the consistency of

the RDE experiments and thereby determine the electron transferred, $n_{e^-}$ and $H_2O_2$ percentages. They were found to be in agreement.

**S4:** The improved stability of PtPd/$Ni_{12}P_5$ catalysts is attributed not only to the stability of the components (Ni, P, Pt, Pd) individually but also to the interactions between $Ni_{12}P_5$ and PtPd that effectively reduce the passivation of the nanoparticles. $Pt_1Pd_2(7.5)/Ni_{12}P_5$ underwent negligible change in activity with the introduction of 1M MeOH (**Figure S30a**). Chronoamperometric study for a period of 3 hours resulted in a sudden drop in current for Pt while no such change was observed for $Pt_1Pd_2(7.5)/Ni_{12}P_5$ (**Figure S30b**). This indicates that catalytic instability of Pt/C towards ORR in presence of MeOH occurs due to methanol oxidation.

**S5:** $Pt_1Pd_2(7.5)/Ni_{12}P_5$ at 1600 rpm exhibited an onset of 1.0 V and $E_{1/2}$ of ca. 0.9 V with a maximum diffusion limited current density of 6.5 mA/cm$^2$ at 0.1 V. The slight shift in the onset and $E_{1/2}$ values in acidic media, as compared to the alkaline case, is expected in the case of metal-based systems.[24] Tafel plots near low current density (potential range 0.85-1.05 V), near onset of the ORR, (**Figure S33a**) show that the obtained values for $Pt_1Pd_1(7.5)/Ni_{12}P_5$ and $Pt_2Pd_1(7.5)/Ni_{12}P_5$ are consistent with the representative values of Tafel slopes for Pt catalysts in previously reported work[4,7] and confirms a similar ORR mechanism. EIS data reveals the presence of ohmic resistance ($R_e$), charge transfer resistance ($R_{CT}$) and Warburg impedance (**Figure S33b, S34** and **Table S5)**. The slightly higher $j_d$ value @ 1600 rpm (than the theoretical 5.7 mA/cm$^2$ mark for 4e$^-$ reduction) may be arising from the efficiency of the selective direct pathway,[24] which was probed by RRDE measurements.

**S6:** The broad oxidative peak at 1.3V is due to the in-situ generated oxide/hydroxide species generated during OER. Lattice fringe with interplanar spacing of 0.218 nm can be ascertained to specific facets of nickel oxo/hydroxo species (**Figure S35**). The reduced $R_{ct}$ value of $Pt_1Pd_2(7.5)/Ni_{12}P_5$ is also indicative of increased charge-transfer kinetics (**Figure 4b, S36** and **Table S6**). Stability is yet another important factor in evaluating the electrochemical performance of a catalyst. $Pt_1Pd_2$ (7.5)/ $Ni_{12}P_5$ remains stable for 6000 cycles after running potential CV scans from 0.06 to 1.1 V vs RHE (**Figure S37**). **Figure 4c** shows the comparison of Tafel slopes for all the catalysts.

**S7:** Inspired by the enhanced ORR activity of $Pt_1Pd_2(7.5)/Ni_{12}P_5$ being close to Pt/C in the half cell reaction, its potential as a cathode material for proton-exchange menbrane fuel cell (PEMFC) has been performed. The efficiency of $Pt_1Pd_2(7.5)/Ni_{12}P_5$ not only acts as a bifunctional catalyst but also proved to be a potential cathode material for PEMFC which is comparable to Pt/C, thereby demonstrating its activity for real applications. This work highlights the importance of the rational designing of nanostructures with favourable interactions for development of novel low-Pt ORR catalysts. The best catalyst in this study succeeded in reducing precious metal loding by 81% compared to the commercial Pt/C, which invokes the potential impact of this material in terms of its economical benefits and commercial application. A comparison of all the reported TMP electrocatalysts with our best catalyst is summarized in **Table S7,** which also clearly highlights the potential of this material, especially as the conventional carbon-supported MEAs fall short of meeting durability target of PEMFCs in the automotive industry.

**References**


1 L. Zang, M. Wei and S. Wang, Z. Li, L. X. Ding, H. Wang, *Chem. Sci*., 2015, **6**, 3211-3216.

2 H. Duan and C. Xu, *Electrochim. Acta*, 2015, **152**, 417-424.

3 Y. Zheng, J. Qiao, J. Yuan, J. Shen and A. J. Wang, *Nanotechnology*, 2018, **29**, 10LT01.

4 J. Wu, H. Shan, H. Cronk, F. Chang, H. Kareem, Y. Zhao, J. Luo, V. Petkov and C. J. Zhong, *J. Phys. Chem. C*, 2017, **121**, 14128−14136.

5 H. S. Chen, Y. T. Liang, T. Y. Chen, Y. C. Tseng, C. W. Liu, S. R. Chung, C. T. Hsieh and C. E. Lee, K. W. Wang, *Chem. Commun*., 2014, **50**, 11165-11168.

6 H. Wei, Z. Y. Hu, Y. X. Xiao, G. Tian, J. Ying, G. V. Tendeloo, C. Janiak, X. Y. Yang and B. L. Su, *Chem. Asian J.*, 2018, **13**, 1119–1123.

7 J. Choi, J. Cho, C. W. Roh, B. S. Kim, M. S. Choi, H. Jeong, H. C. Ham and H. Lee, *Appl. Catal. B: Environmental*, 2019, 142-149.

8 F. Godínez-Salomón, C. P. Rhodes, K. S. Alcantara, Q. Zhu, S. E. Canton, H. A. Calderon, J. L. Reyes-Rodríguez, M.A. Leyva and O. Solorza-Feria, *Electrochim. Acta*, 2017, **247**, 958-969.

9 J. Y. Park, D. H. Kwak, K. B. Ma, S. B. Han, G. S. Chai, S. K. Kim, D. H. Peck, C. S. Kim, A. Kucernak and K. W. Park, *J. Catal*., 2018, **359**, 46-54.

10 K. A. Kuttiyiel, K. Sasaki, G. G. Park, M. B. Vukmirovic, L. Wu, Y. Zhu, J. G. Chen and R. R. Adzic, *Chem. Commun*., 2017, **53**, 1660–1663.

11 C. Fan, G. Wang, L. Zou, J. Fang, Z. Zou and H. Wang, *J. Power Sources*, 2019, **429**, 1-8.

12 J. H. Lim, H. Shin, M. J. Kim, H. Lee, K. S. Lee, Y. K. Kwon, D. H. Song, S. K. Oh, H. Kim and E. A. Cho, *Nano Lett*., 2018, **18**, 2450−2458,

13 C. Li, T. Liu, T. He, B. Ni, Q. Yuan and X. Wang, *Nanoscale*, 2018, **10**, 4670-4674.

14 X. Huang, Z. Zhao, L. Cao, Y. Chen, E. Zhu, Z. Lin, M. Li, A. Yan, A. Zettl, Y. M. Wang, X. Duan, T. Mueller and Y. Huang, *Science*, 2015, **348**, 1230–1234.

15 T. Kwon, M. Jun, H. Y. Kim, A. Oh, J. Park, H. Baik, S. H. Joo and K. Lee, *Adv, Func. Mater*., 2018, **28**, 1706440.

16 Y. Jin, D. Han, W. Jia, F. Li, X. Chen, G. Huang and D. Zhang, *Int. J. Electrochem. Sci*., 2017, **12,** 6535 – 6544.

17 J. H. Jang, E. Lee, J. Park, J. Kim, S. Hong and K. Y. Kwon, *Sci. Rep.*, 2013, **3**, 2872.

18 Y. Deng, H. Xue, S. Lu, Y. Song, X. Cao, L. Wang, H. Wang, Y. Zhao and H. Gu, *ACS Appl. Energy Mater*., 2018, **1**, 4891−4898.

19 N. Todoroki, T. Kato, T. Hayashi, S. Takahashi and T. Wadayama, *ACS Catal.,* 2015, **5**, 2209−2212.

20 X. Zhao, C. Xi, R. Zhang, L. Song, C. Wang, J. S. Spendelow, A. I. Frenkel, J. Yang, H. L. Xin and K. Sasaki, *ACS Catal.*, 2020, **10**, 10637-10645.

21 M. Gong, D. Deng, D. Xiao, L. Han, T. Zhao, Y. Lu, T. Shen, X. Liu, R. Lin, T. Huang, G. Zhou, H. Xin and D. Wang, *ACS Catal*., 2019, **9**, 4488−4494